NUMERICAL SOLUTION OF CYLINDRICAL CAVITY EXPANSION IN SANDS: EFFECTS OF FAILURE CRITERIA AND FLOW RULES

By

BRENTON RYAN COOK

A thesis submitted in partial fulfillment of

the requirements for the degree of

MASTER OF SCIENCE IN CIVIL ENGINEERING

WASHINGTON STATE UNIVERSITY

Department of Civil and Environmental Engineering

December 2010

To the Faculty of Washington State University:

The members of the Committee appointed to examine the thesis of BRENTON RYAN COOK find it satisfactory and recommend that it be accepted.

Balasingam Muhunthan, Ph.D., Chair

William Cofer, Ph.D.

Haifang Wen, Ph.D.

ACKNOWLEDGEMENTS

I would first like to thank Dr. Balasingam Muhunthan for his support, guidance and enthusiasm concerning this study and my future in the field of geotechnical engineering. To my family, thank you for keeping me going over the past six years; financially and motivationally. Thank you to my fellow graduate students for their support, specifically Gonzalo Montalva for his frequent and much appreciated technical guidance. Last, but not least, I want to thank the Department of Civil Engineering at Washington State University for the financial support provided during the course of this study while also providing me with a strong academic foundation for future endeavors.

NUMERICAL SOLUTION OF CYLINDRICAL CAVITY EXPANSION IN SANDS: EFFECTS OF FAILURE CRITERIA AND FLOW RULES

Abstract

by Brenton Ryan Cook, M.S.
Washington State University
December 2010

Chair: Balasingam Muhunthan

Cavity expansion in soil is an important area of interest within the field of geotechnical engineering. Detailed understanding of this boundary value problem would allow engineers to better interpret in-situ test data from devices such as the pressuremeter and the cone penetrometer. Cavity expansion theory can also be extended to important and complex design problems commonly encountered in practice such as driven/cast in place lateral pile capacities, in addition to applications for tunneling.

Early research into cavity expansion in soils involved developing closed form solutions for clays assuming linear elastic, perfectly plastic behavior. Later, rigorous analytical solutions for the cavity expansion problem were introduced which made a concerted effort to capture the effects of confinement pressure and density to characterize the behavior of sands. More recently, finite difference models have been presented that are more versatile for conducting studies on the influence of various parameters on cavity expansion.

A recent finite difference model proposed by researchers from Purdue University discretized the plastic region around an expanding cavity into thin shell elements. Iterations across each shell were carried out using an empirical friction angle relation in conjunction with a flow rule and failure criterion. Recognizing that there exist numerous friction angle models, flow rules and failure criteria, it is of interest to investigate how their combinations influence results when implemented into a cavity expansion analysis.

This study modified the finite difference model with the objective of investigating the influence of different friction angle models, flow rules and failure criteria within a cylindrical cavity expansion algorithm for sand assuming drained conditions. Results from the proposed algorithm were evaluated including limit pressures for different combinations of depth and relative density. It was found that the choice of flow rule had little impact on predicted results, whereas the choice of failure criterion did have influence. Recognition of such modeling nuances allows for algorithms, such as the one presented in this study, to predict soil conditions in the field with increased confidence.

TABLE OF CONTENTS

Page

LIST OF TABLES

Page

List of Figures

CHAPTER 1

INTRODUCTION

1.1 Introduction

The expansion of cylindrical or spherical cavities in an infinite medium is one of the basic boundary value problems in solid mechanics (Carter et al. 1986, Palmer 1972). The solution to such problems has been of interest in the area of geomechanics where they have been used to develop approximate analyses of the stresses and deformations induced by tunnels and driven piles and also to interpret the results of in-situ penetration tests such as cone penetrometer and pressuremeter (see appendix A). For applications involving the cone penetrometer and driven piles, the cavity initially has zero radius and the resulting strains are large. For most pressuremeter applications, the initial radius is finite and induced strains are generally small except for full displacement pressuremeters where the initial radius is again taken to be zero.

The classical solutions for the cavity expansion problem often use rigid plastic models for material behavior. However, these models do not account for changes in volume associated with dilatant soils thus their applicability is limited to undrained clays and fine grained soils. Most soils, especially sands when subjected to shear experience significant volume changes that need to be accounted for within the analyses.

The mechanical behavior of soils and other particulate materials is strongly influenced by the packing of individual particles. Consequently, some type of index measure such as void ratio or relative density is needed to provide information on the state of packing. Most often in geotechnical practice, the initial state of sands and invariably the mechanical behavior is described with respect to the degree of looseness or denseness of sands quantified through these basic measures. However, it is now known that the mechanical behaviour of soil is very sensitive to the combination of changes in volume and the confining stress. This information must be incorporated to properly describe the mechanical behavior of soils.

Several measures that combine the effect of volume and effective stress have been proposed in the literature. The pioneering contribution to this direction of thought was the introduction of the critical state soil mechanics framework (Schofield & Wroth 1968). Critical state soil mechanics showed that soils attain a unique critical state line with prolonged shearing and that this state could be used to distinguish shear behaviour. It was further shown that soil behaviour can be normalized using the parameter $v_\lambda = v + \lambda \ln p$, where v is the specific volume, p is the mean stress and λ is a material property. The parameter v_λ represents the intercept in v-lnp space for a particular stress ratio.

The state parameter models of Been & Jefferies (1985, 2006) and Jefferies (1993) provide useful measures to describe the state of sand well. Been & Jefferies (1985) demonstrated that experimental data strongly suggested that the behaviour of sands depended on the *difference* ξ, termed the state parameter, between the void ratio e and e_{cs} where e_{cs} is the value of the void ratio at the critical state evaluated at the same effective pressure*;* see also Jefferies & Been (2006) for a textbook account. It can be shown that v_λ and the state parameter ξ are related by $\xi = v_\lambda - \Gamma$, where Γ is the intercept of the critical state line in v-lnp space.

Since soil strength has been shown to be dependent upon a combination of volume and stress conditions, researchers have developed empirical models which correlated density measures with the angle of internal friction using test data. Bolton (1986) proposed a linear model which related relative density and mean stress to predict the mobilized friction angle for different sands. Been & Jefferies (1985) also observed strong trends when the state parameter ξ was plotted with corresponding values of peak mean stress which led to their own empirical model. Lancellotta (1995) has shown that v_λ correlates well with the strength of sands. This study explores the applicability of v_λ to predict values of the mobilized friction angle.

Generally, the classical Mohr-Coulomb failure criterion is chosen to model the strength behavior of soils. This criterion ignores the intermediate stress and thus only recognizes the contribution from the minor and major principal stresses. In order to quantify the effects of the intermediate stress, Matsuoka & Nakai (1974) introduced the SMP failure criterion which accounts for all three principal stresses. This study will implement both the aforementioned failure criteria to assess any differences when applied to a plane strain cavity expansion model.

There have been several advances made to the rigid plastic model assumption in the solution of cavity expansion problems as applied to sands. Carter et al. (1986) solved the problem for the expansion of spherical and cylindrical cavities in an elastic-plastic material, yielding according to a Mohr-Coulomb material model but with a non associated flow rule to account for volume changes. The dilation and internal friction angles are hence generally different. However, these material properties were assumed as constant and independent of deformation history. Collins et al. (1992) have made a significant improvement to the cavity expansion analysis in sands where the sand properties were modeled using Been & Jefferies (1985) state parameter in which the values of friction and dilation angles depended on the deformation history. These researchers developed analytical solutions that provided the void ratio and stress state as a function of the ratio of the radius of the point under consideration to the cavity radius.

Salgado and his colleagues in a series of papers (1997, 2001, 2007) have tried to solve the spherical and cylindrical cavity expansion problem by introducing a finite difference algorithm that provided comparable results to the analytical solution presented by Collins et al. (1992). Salgado's model assumes expansion from an initial cavity radius of zero and divides the plastic zone into thin incremental shells which allows the friction angle to change as a function of either the relative index relations developed by Bolton (1986) or that of the state parameter of Been & Jefferies (1985). Radial, hoop and volumetric large strain relations were combined with a flow rule in order to track deformation within the plastic zone for plane strain conditions. Salgado used the flow rule developed by Rowe (1962) for the expansion analysis, but there exist several alternatives to Rowe's flow rule that can be implemented just as easily into the model.

This study used the finite difference method to explore the effects of varying flow rules and failure criteria within a cylindrical cavity expansion algorithm. Empirical friction angle models were also varied and this study utilized v_λ as a state measure in addition to the state parameter ξ. The objectives of this study were as follows:

1. Develop a large strain numerical solution for cylindrical cavity expansion.

2. Interpret results from the cavity expansion algorithm in which the angle of internal friction is governed by v_λ.

3. Compare predicted values of the limit pressure with measured values to assess the performance of the cavity expansion algorithm.

4. Investigate the effects of the different combinations of the empirical friction angle model, failure criterion and flow rule on cavity expansion results.

1.2 Organization of Thesis

Chapter 2 presents an overview of sand behavior under shear using critical state soil mechanics. The discussion includes a description of measures of density, strength correlations and dilatancy concepts. A modified version of the cavity expansion algorithm presented by Salgado et al. (2001, 2007) is covered in detail within Chapter 3. Compatibility relations for stresses and strains plus basic cavity expansion concepts are detailed as they apply to the cavity expansion algorithm. Results from the algorithm are discussed in Chapter 4. A comparative analysis between limit pressure results obtained from the cavity expansion algorithm and measured values is presented. Next, cavity expansion results obtained using v_λ to control the behavior of the internal friction angle are assessed as well as the consequences of implementing different flow rules, friction angle models and failure criteria. Chapter 5 presents conclusions and offers recommendations for future research related to this study.

CHAPTER TWO

SHEAR BEHAVIOR OF SANDS

2.1 Critical State Soil Mechanics

Critical state soil mechanics (CSSM) (Schofield & Wroth, 1968) is a framework which recognizes that soil is a collective of interlocking frictional particles. The fundamental concept behind CSSM asserts that soil behavior when subjected to shear depends on density *and* effective stress conditions (Schofield 1998, 2005). Detailed accounts of the basic principles, the features, and finite element applications of the CSSM framework have been presented in a number of publications. The two invariant stress parameters used in CSSM are the mean normal effective stress

$$p' = \frac{1}{3}(\sigma'_1 + \sigma'_2 + \sigma'_3) \tag{2-1}$$

and the deviator stress

$$q = \frac{1}{\sqrt{2}}\sqrt{(\sigma'_2 - \sigma'_3)^2 + (\sigma'_3 - \sigma'_1)^2 + (\sigma'_1 - \sigma'_2)^2} \tag{2-2}$$

where σ'_1, σ'_2, and σ'_3 are the principal effective compressive stresses. This study is restricted to drained conditions which implies that pore pressures are zero. Thus, total stresses will be equivalent to effective stresses and the prime notation is not necessary from this point forward. Ground stresses at depth can be represented by triaxial conditions where σ_2 and σ_3 are taken to be equivalent. Therefore Eqns. 2-1 and 2-2 can be reduced to:

$$p = \frac{1}{3}(\sigma_1 + 2\sigma_3) \tag{2-3}$$

$$q = \sigma_1 - \sigma_3 \tag{2-4}$$

In addition, a third variable, the specific volume v, which is a variant of the void ratio, e, is used to track volumetric changes within a soil:

$$v = 1 + e \tag{2-5}$$

When used collectively, p, q, and v define the state of a soil specimen.

Roscoe et al. (1958) published findings for a series of large strain triaxial tests on clay. They observed that the ultimate state of any soil specimen will eventually lie on a critical state line (CSL) as shown in Figure 2-1. It was found that each soil attained a unique CSL independent of its initial state before shearing was induced. In order to satisfy having reached the CSL, the parameters p, q and v of a soil specimen must remain constant as strains continue to increase.

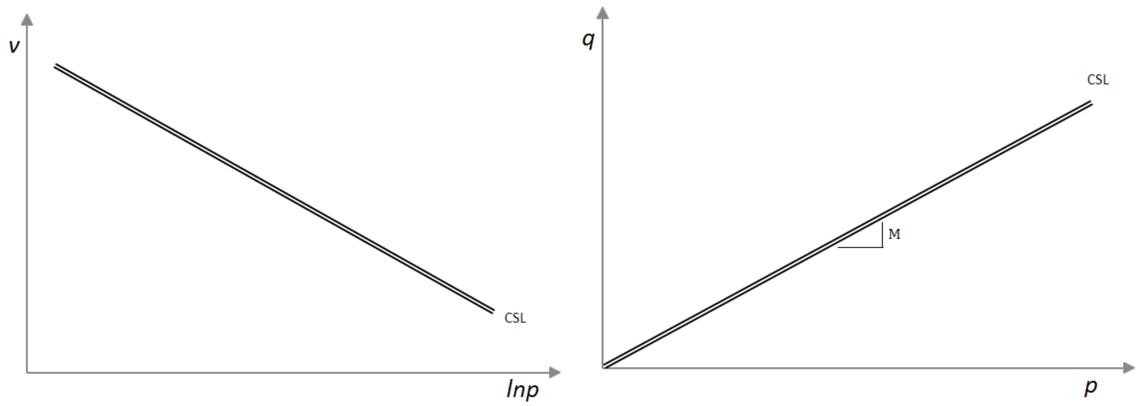

(a) (b)

Figure 2-1: Critical state line in v-lnp and q-p space.

The critical state line is typically shown as a set of two parallel lines to signify the conditions that *both* stress and volume changes have reached ultimate state conditions. Roscoe et al. (1958) noted that the critical state line could be represented as linear in v-lnp space thus:

$$v = \Gamma - \lambda \ln p \tag{2-6}$$

Γ and λ in the preceding equation are material dependent parameters. Γ is the intercept of the CSL, typically taken at p = 1 kPa, and λ is the slope. Eq. 2-6 can also be expressed using void ratio, but it must be recognized that values of Γ will change accordingly. Furthermore, Γ and λ are unit sensitive, and this study opts to use metric units exclusively.

The critical state line in q-p space is represented by:

$$q = Mp \tag{2-7}$$

where M is the internal friction of the soil. CSSM uses the stress ratio η to quantify the amount of shear stress within a soil. η is defined as:

$$\eta = \frac{q}{p} \quad \text{"Triaxial"} \tag{2-8}$$

$$\eta = \frac{t}{s} \quad \text{"Biaxial"} \tag{2-9}$$

Where t and s are the deviator and mean stresses respectively for bi-axial loading conditions.

$$t = \frac{1}{2}(\sigma_1 - \sigma_3) \tag{2-10}$$

$$s = \frac{1}{2}(\sigma_1 + \sigma_3) \tag{2-11}$$

For isotropic stress conditions, the deviator stress is zero and so is η. With an increase in shear stress, the value of η will increase until reaching the critical state stress ratio M. Figure 2-1 (b) shows the CSL in stress space with slope represented by M. Most commonly, researchers have used test data and the Mohr-Coulomb failure criterion to obtain M. M is sensitive to whether bi-axial or triaxial conditions are present and equations for the triaxial and bi-axial critical friction ratios (M_{TX} and M_{BX}) are as follows:

$$M_{TX} = \frac{q}{p} = \frac{{}^{\sigma_1}\!/_{\sigma_3} - 1}{\frac{1}{3}\left({}^{\sigma_1}\!/_{\sigma_3} + 2\right)} \tag{2-12}$$

$$M_{BX} = \frac{t}{s} = \frac{{}^{\sigma_1}\!/_{\sigma_3} - 1}{{}^{\sigma_1}\!/_{\sigma_3} + 1} \tag{2-13}$$

The Mohr-Coulomb failure envelope for sands is:

$$\frac{\sigma_1}{\sigma_3} = \frac{1 - \sin\text{ø}}{1 + \sin\text{ø}} \tag{2-14}$$

If Eqns. 2-12 and 2-13 are combined with 2-14, the critical friction ratio can be expressed as a function of the critical state friction angle $ø_{cs}$.

$$M_{TX} = \frac{6\sin\phi_{cs}}{\sin\phi_{cs} + 3} \tag{2-15}$$

$$M_{BX} = \sin\phi_{cs} \tag{2-16}$$

A soil specimen that has undergone isotropic consolidation will initially fall on the normal consolidation line (NCL) before shearing is induced. The NCL is taken to be parallel to the CSL as shown in Figure 2-2 and is represented by the equation:

$$v = N - \lambda \ln p \tag{2-17}$$

The NCL and CSL represent plastic deformation of the soil and will have a material dependent slope λ. When a soil is unloaded, elastic rebound occurs along the elastic compression line:

$$v = v_\kappa - \kappa \ln p \tag{2-18}$$

The material dependent slope of the elastic compression line is κ with an intercept equal to v_κ. To illustrate how the elastic and plastic compression lines interact, assume that a soil specimen is being isotropically consolidated under triaxial conditions. Test conditions are assumed to start at point 1 in Figure 2-2. As confining stress is increased, the mean stress increases and the specific volume decreases due to consolidation until point 2 is reached. At point 2, the confining pressure is reduced and the soil specimen is allowed to swell along the elastic compression line until reaching equilibrium at point 3. If stresses are again increased isotropically, the sample will continue back down the elastic compression line towards point 2 then continue down the NCL until point 4 is reached. At point 4, the confining pressure can again be reduced to allow the sample to swell to point 5. Every time additional plastic volume change occurs along the NCL, the elastic compression line is shifted downward by the same amount.

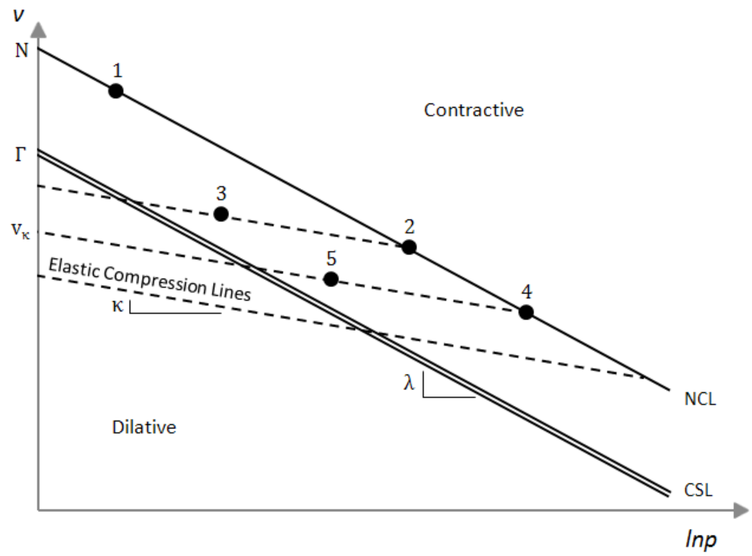

Figure 2-2: Normal, critical and elastic compression lines in v-lnp space.

Before a typical drained triaxial test begins, the soil sample is consolidated to an isotropic stress state which means that η for triaxial conditions is equal to zero. When the drained test is initiated, the axial stress is increased and as a result the deviator stresses imposed on the sample increase from zero. For states between the NCL and CSL, there exist η-lines which represent different states of deviator stress as shown in Figures 2-3 and 2-4.

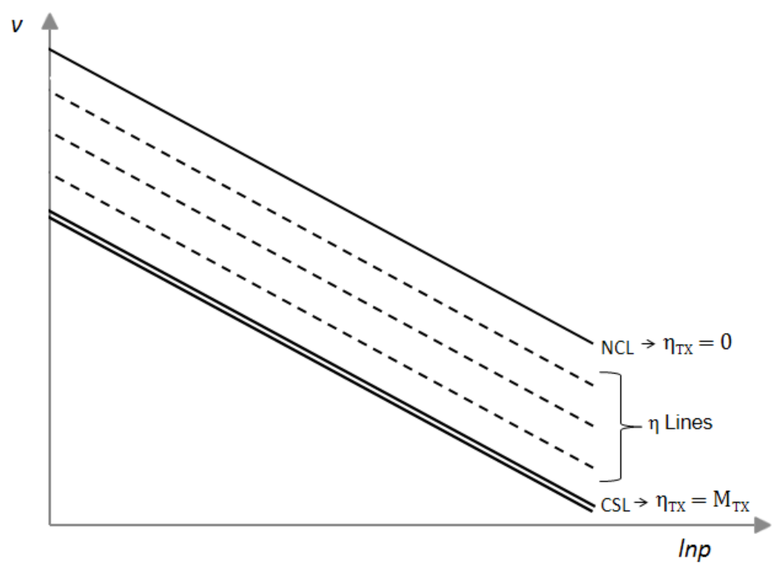

Figure 2-3: η-lines in v-lnp space.

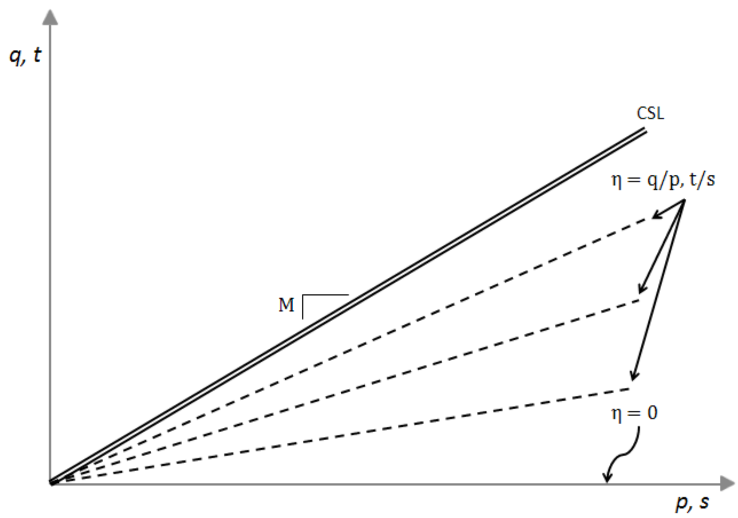

Figure 2-4: η-lines in stress space.

This study assumes that bi-axial and triaxial friction angles are equivalent, although this is not the case in reality. Past testing by researchers has shown that the friction angle obtained from plane strain testing is slightly larger than the triaxial friction angle by a ratio of approximately 9:8 (Wroth 1984). Researchers have argued that this difference is small enough to neglect as it would not contribute significantly to the yield behavior of a material (Collins et al. 1992). Furthermore, bi-axial and plane strain behavior are not equivalent from a mechanical standpoint, but friction angles from either condition are also assumed to be equivalent in this study.

2.2 Measures of Density

In order to understand engineering behavior of a soil, volumetric ratios and index properties such as the void ratio and relative density D_r are commonly employed in geotechnical practice.

$$e = \frac{V_v}{V_s} \tag{2-19}$$

$$D_r = \frac{e_{max} - e}{e_{max} - e_{min}} \tag{2-20}$$

V_v and V_s in the equation for e represent the volume of voids and the volume of solids respectively within a soil mass. Relative density assesses the current state void ratio with respect to inherent maximum and minimum void ratios (e_{max} and e_{min}) in order to measure the degree of looseness or denseness of the packing of a soil structure. Currently, relative density is used to parameterize a broad range of geotechnical testing procedures. But, it is not sufficient to provide engineers with sufficient information as to how a soil may behave due to the effects of confinement. As such, alternative approaches for quantifying density states have been proposed.

As mentioned in the introduction, Schofield and Wroth used the CSSM framework to derive the parameter v_λ which represents the intercept for an η-line in v-lnp space (p = 1 kPa).

$$v_\lambda = v + \lambda \ln p \tag{2-21}$$

This parameter incorporates the contributions of both density and confining stress as opposed to D_r which can only capture density states. The value of v_λ represents a point within v-lnp space thus requires a reference point to be meaningful when describing the relative state of packing for a soil.

The state parameter ξ proposed by Been & Jefferies (1985) is another measure that combines both volume and density. Been and Jefferies' state parameter is defined as:

$$\xi = e - e_{cs} = v - v_{cs} \tag{2-22}$$

The variables e_{cs} and v_{cs} in Eq. 2-22 represent the void ratio and specific volume along the critical state line at a specific value of mean stress and has the equation:

$$v_{cs} = \Gamma - \lambda \ln p \tag{2-23}$$

The state parameter is an attractive measure in the sense that it provides engineers with the ability to predict whether a soil will be partial to either contractive or dilative volumetric behavior under variable stress conditions as shown in Figure 2-5. Negative values of ξ indicate that a soil is on the dilative side of critical, whereas positive values are on the contractive side. Normalizing effects were also observed when using the state parameter to compare properties of sands. This meant that sands with varying material characteristics displayed the same engineering behavior when prepared at similar values of ξ.

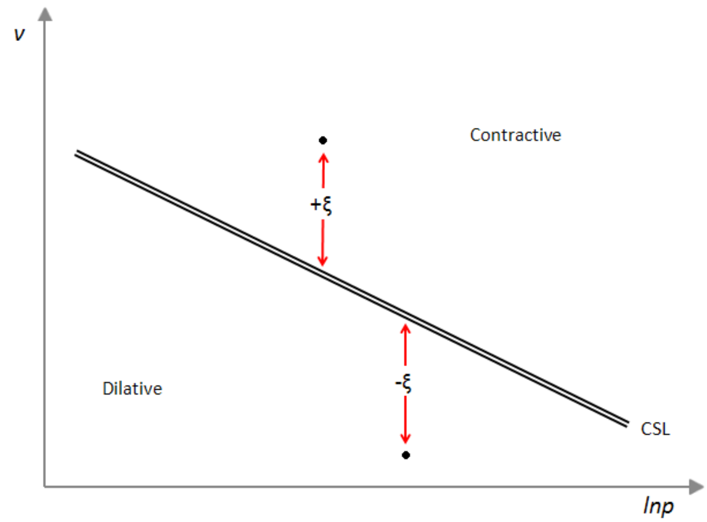

Figure 2-5: State parameter in v-lnp space.

If the CSL, NCL and η-lines are assumed to be parallel in v-lnp space, the parameters are related by:

$$\xi = v_{\lambda} - \Gamma \tag{2-24}$$

Figure 2-6 illustrates this relationship between the two variables.

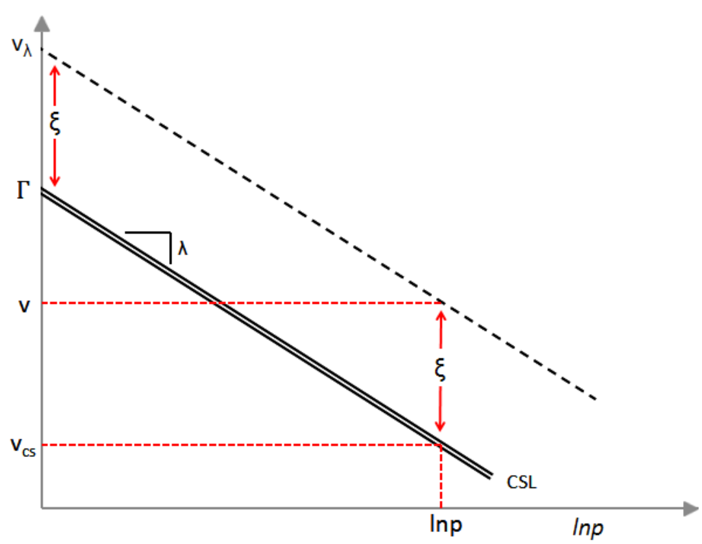

Figure 2-6: Relationship between v_{λ}, Γ, and ξ in v-lnp space.

2.3 Correlations between State Parameters and Internal Friction Angle

D_r, ξ and v_λ have been used to quantify several different engineering properties of a soil mass. This study is focused on the friction angle ø of sands. Been & Jefferies (1985) have compiled an extensive database of drained and undrained triaxial tests on sands. Strong trends were observed when experimental values of peak friction angle were plotted as a function of ξ. An empirical relation was developed to predict ø as a function of the state parameter ξ and critical state friction angle $ø_{cs}$.

$$ø = A[\exp(-\xi) - 1] + ø_{cs} \qquad (2\text{-}25)$$

The constant A in Eq. 2-25 varies depending on the material type and if triaxial or plane strain conditions are in place. The preceding relation has been employed in studies by Salgado et al. (2001, 2007) and Hao et al. (2010).

Bolton (1986) developed an empirical model that correlates ø with D_r and $ø_{cs}$. The model is based upon a compilation of triaxial data for eight different sands. Bolton expressed his relation using a state parameter termed the relative dilatancy index I_R.

$$I_R = D_r(Q + \ln p) - R_Q \qquad (2\text{-}26)$$

$$ø = ø_{cs} + 3I_R \qquad \text{“Triaxial”} \qquad (2\text{-}27)$$

$$ø = ø_{cs} + 5I_R \qquad \text{“Plane Strain”} \qquad (2\text{-}28)$$

Bolton recommended using values of 10 and 1 for the regression constants Q and R_Q.

Lancellotta (1995) showed that v_λ correlated linearly with the peak friction angle as shown in Figure 2-7; accordingly the following linear relation can be developed:

$$ø = c - mv_\lambda \qquad (2\text{-}29)$$

or using Eq. 2-21:

$$ø = c - m(v + \lambda \ln p) \qquad (2\text{-}30)$$

The material constants m and c for Ticino sand were found to be 44.80 and 116.61 using the data provided in Figure 2-7. For this study, Eq. 2-29 will be used in place of the previous empirical correlations developed by Bolton (1986) and Been & Jefferies (1985) which are functions of either D_r or ξ.

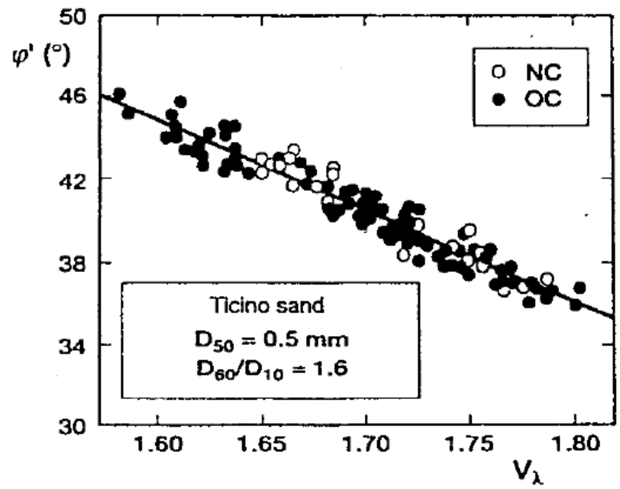

Figure 2-7: ø versus v_λ for Ticino sand (after Lancellotta 1995).

2.4 Failure Criteria

The classical Mohr-Coulomb failure criterion for sands is of the form:

$$\frac{\sigma_1 - \sigma_3}{\sigma_1 + \sigma_3} = \sin\text{ø} \tag{2-31}$$

Eq. 2-31 can be easily rearranged to form an expression for the ratio of major to minor principal stresses:

$$N = \frac{\sigma_1}{\sigma_3} = \frac{1 + \sin\text{ø}}{1 - \sin\text{ø}} \tag{2-32}$$

Eq. 2-32 is termed the "stress ratio at failure" and is denoted by N. One well known limitation involved with using the Mohr-Coulomb failure criterion is that it neglects any effects contributed by the intermediate stress σ_2. Despite this limitation, the geotechnical community commonly uses the Mohr-Coulomb failure criterion because of its simplicity.

Several failure criteria that account for intermediate principal stresses have been proposed (Matsuoka & Nakai 1974, Lade & Duncan 1975). Matsuoka introduced the concept of the spatial mobilized plane (SMP) on which failure is assumed to occur. The resulting failure criterion is of the form (Wroth 1984, Griffiths & Huang 2009):

$$\frac{I_1 I_2}{I_3} = 9 + 8\tan^2 \phi = B \tag{2-33}$$

I_1, I_2, and I_3 in Eq. 2-33 are stress invariants expressed in terms of all three principal stresses:

$$I_1 = \sigma_1 + \sigma_2 + \sigma_3 \tag{2-34}$$

$$I_2 = \sigma_2\sigma_3 + \sigma_3\sigma_1 + \sigma_1\sigma_2 \tag{2-35}$$

$$I_3 = \sigma_1\sigma_2\sigma_3 \tag{2-36}$$

Figure 2-8 displays both the Mohr-Coulomb and SMP failure envelopes in 3-D stress space.

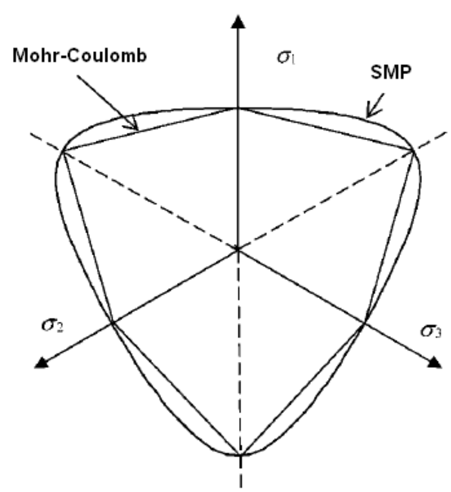

Figure 2-8: Mohr-Coulomb and SMP failure envelopes

(modified after Griffiths & Huang 2009).

Bishop (1966) introduced the parameter b which provides a measure of the intermediate principal stress with respect to the maximum and minimum principal stresses.

$$b = \frac{\sigma_2 - \sigma_3}{\sigma_1 - \sigma_3} \tag{2-37}$$

Griffiths & Huang (2009) showed that Eq. 2-37 can be rearranged in terms of σ_2 then substituted into the SMP criterion (Eq. 2-33) to obtain:

$$(b + b^2)\left(\frac{\sigma_1}{\sigma_3}\right)^3 + (2 + 4b - Bb - b^2)\left(\frac{\sigma_1}{\sigma_3}\right)^2 + (Bb - b^2 - 2b + 5)\frac{\sigma_1}{\sigma_3} + b^2 - 3b + 2 = 0 \tag{2-38}$$

It was then shown that the stress ratio at failure N could be obtained by taking the partial derivative of Eq. 2-38 with respect to b then solving the cubic equation using the positive real root to obtain the following expressions which are representative of maximum conditions:

$$N = -\frac{1}{2} + \frac{1}{2}B - \sqrt{B} + \frac{1}{2}\sqrt{\left(\sqrt{B} - 3\right)\left(\sqrt{B} - 1\right)(B - 1)} \tag{2-39}$$

$$b = \frac{1}{2} - \frac{1}{2}\sqrt{\frac{\sqrt{B} - 3}{\sqrt{B} + 1}} \tag{2-40}$$

Figure 2-9 shows plots of N versus the angle of internal friction ø for either criterion defined by Eqns. 2-32 and 2-39. It is apparent from Figure 2-9 that the Mohr-Coulomb criterion is slightly more conservative when predicting soil strengths.

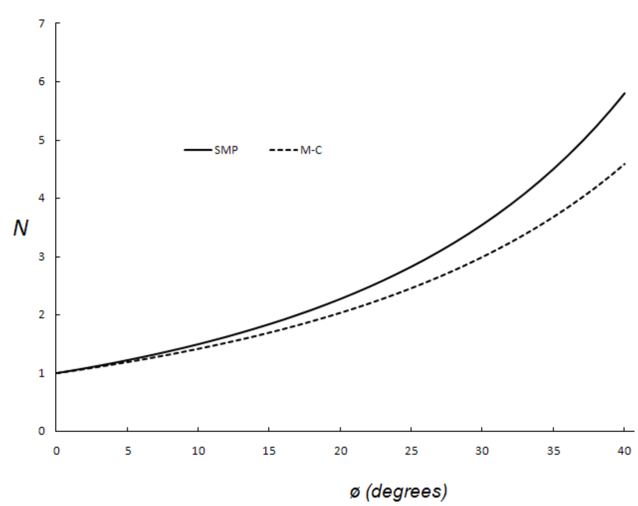

Figure 2-9: Flow number versus angle of internal friction.

2.5 Energy Dissipation in Soils and Flow Rules

Taylor (1948) was the first to use work principles to describe the shear behavior of sands. Figure 2-10 shows the schematic of a direct shear box test which Taylor used in his analysis. If a soil is prepared in a dense state, the individual soil grains will be oriented such that lateral translation dx can only occur if the grains roll over each other which results in vertical dilation dy of the soil mass. Note, this assumes that elastic deformation and the effects of particle crushing are negligible, thus the behavior is plastic. If dy is sufficiently small compared to dx, the dilation that accompanied shear deformation can be described using a dilatancy angle ψ as:

$$\psi = \frac{dy}{dx} \tag{2-41}$$

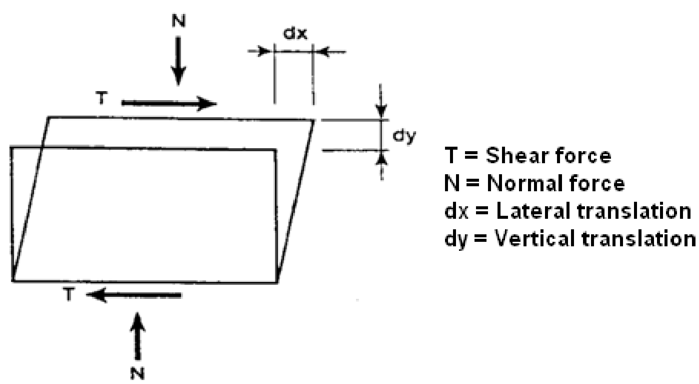

Figure 2-10: Dilation under direct shear box conditions (modified after Lancellotta 1995).

For the conditions of load and displacement shown in Figure 2-8, the following equation for energy balance was developed:

$$\mu N dx = T dx - N dy \tag{2-42}$$

where μ represents the coefficient of static friction. Eq. 2-42 can be rearranged to include the contribution due to dilatancy:

$$\frac{T}{N} = \mu + \frac{dy}{dx} = \mu + \psi \tag{2-43}$$

Taylor's thermomechanical approach to describe the plastic deformation of soils under shear was adopted by many researchers. The dilatancy ratio of a material is the ratio of the volumetric strain to the deviator strain and is expressed as:

$$\frac{\delta\varepsilon_v}{\delta\varepsilon_s} = \frac{\delta\varepsilon_1 + 2\delta\varepsilon_3}{\frac{2}{3}(\delta\varepsilon_1 - \delta\varepsilon_3)} \qquad \text{“Triaxial”} \qquad (2\text{-}44)$$

$$\frac{\delta\varepsilon_v}{\delta\varepsilon_s} = \frac{\delta\varepsilon_1 + \delta\varepsilon_3}{\delta\varepsilon_1 - \delta\varepsilon_3} \qquad \text{“Bi-axial”} \qquad (2\text{-}45)$$

The variables $\delta\varepsilon_1$, $\delta\varepsilon_3$, $\delta\varepsilon_v$ and $\delta\varepsilon_s$ are the major principal, minor principal, volumetric and deviator incremental strains respectively. Plastic deformation in soil is generally analyzed assuming elastic strains are negligible. Therefore, each equation presented in this section assumes purely plastic behavior. Given that all strains are assumed to be plastic, superscripts will not be used to distinguish between elastic and plastic strains. Drucker (1959) proposed that in order for plastic deformation to be considered stable, the plastic work done by external loading must be positive. Using bi-axial strain notation, Drucker's postulate is represented by the following expression:

$$\delta s \delta\varepsilon_v + \delta t \delta\varepsilon_s \geq 0 \qquad (2\text{-}46)$$

where t is the deviator stress and s is the mean stress represented by:

$$t = \frac{1}{2}(\sigma_1 - \sigma_3) \qquad (2\text{-}47)$$

$$s = \frac{1}{2}(\sigma_1 + \sigma_3) \qquad (2\text{-}48)$$

Plasticity models have customarily assumed equality for the expression above resulting in an associated flow rule as shown in Figure 2-11. The reason is that, if the yield curve is convex as shown in Figure 2-11, stress or strain vectors normal to the yield curve will produce positive work increments.

Two different stress paths in t-s space are displayed in Figure 2-11 and it is shown that any stress point lying within the region bounded by the CSL and the yield curve will deform elastically prior to touching. Past either yield curve, the soil deforms plastically.

Once the yield curve is reached, the stress vector can be modeled as taking a path that is normal to the yield surface in which case it is termed "associative". Alternatively, the plastic flow path can be "non-associated" where the flow path is not normal to the yield surface which is commonly observed in soils as a result of dilatancy effects and the dilation angle ψ.

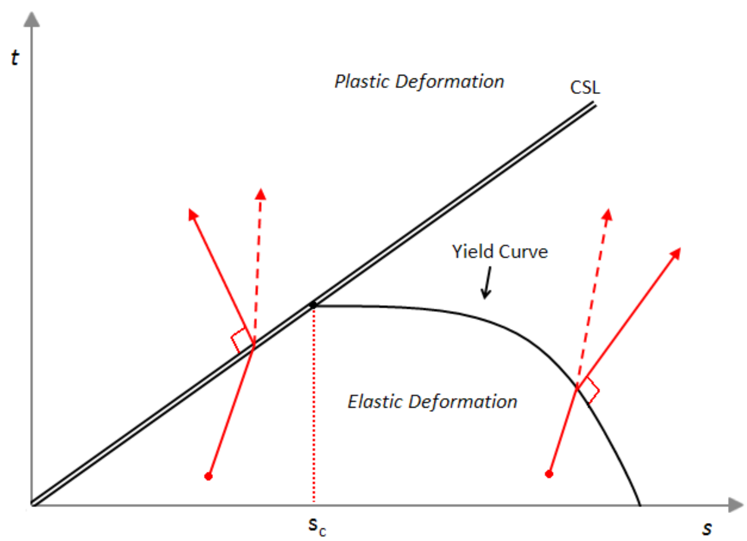

Figure 2-11: Associated flow rule.

Rearranging Drucker's postulate leads to the following expression:

$$\frac{\delta\varepsilon_v}{\delta\varepsilon_s} = -\frac{\delta t}{\delta s} \tag{2-49}$$

Critical state models were the first to utilize the concepts of Drucker's postulate and energy dissipation in the context of an associated flow rule. Subsequently, the term flow rule has been used to loosely refer to relationships of the form in Eqns. 2-44 and 2-45 (see Collins & Muhunthan 2003).

Based on the principles presented by Schofield & Wroth (1968), the energy balance expression for bi-axial conditions is:

$$W = \sigma\delta\varepsilon = s\delta\varepsilon_v + t\delta\varepsilon_s \tag{2-50}$$

Assuming work input is dissipated due to inter-granular friction exclusively:

$$M_{BX} t \delta\varepsilon_s = s\delta\varepsilon_v + t\delta\varepsilon_s \tag{2-51}$$

After some rearrangement, the dilatancy ratio can be expressed as:

$$\frac{\delta\varepsilon_v}{\delta\varepsilon_s} = M_{BX} - \frac{t}{s} = M_{BX} - \eta \tag{2-52}$$

Assuming an associated flow rule as shown by Eq. 2-49, Eq. 2-52 is often referred to as the original cam-clay (OCC) flow rule (Schofield & Wroth 1968) and accordingly:

$$-\frac{\delta t}{\delta s} = M_{BX} - \frac{t}{s} \tag{2-53}$$

Recognizing that t/s in Eq. 2-53 has already been defined as the stress ratio η, differentiation of η provides:

$$\delta\eta = \frac{s\delta t - t\delta s}{s^2} = \frac{\delta t}{s} - \frac{t\delta s}{s^2} \tag{2-54}$$

and after rearrangement:

$$\frac{\delta t}{\delta s} = s\frac{\delta\eta}{\delta s} + \frac{t}{s} \tag{2-55}$$

Schofield then substituted Eq. 2-55 into Eq. 2-53 which results in the following expression:

$$\frac{\delta\eta}{\delta s} = \frac{M_{BX}}{s} \tag{2-56}$$

Upon integration of Eq. 2-56, the equation for the OCC yield curve was obtained:

$$\frac{t}{M_{BX}s} = 1 - \ln\left(\frac{s}{s_c}\right) \tag{2-57}$$

The variable s_c represents the value for the mean stress at the intersection between the CSL and the yield curve as shown in Figure 2-11. The aforementioned process employed by Schofield and Wroth to obtain the OCC yield curve can also be applied to alternative flow rules in order to obtain corresponding expressions for the yield curve.

Rowe (1962) developed a particulate mechanics approach for determining the relation between shear strength and dilation of sands. He proposed that the strength of sand is the result of friction between particle contact points and the amount of energy required for particles to override each other while being sheared. Thus the following expressions were developed which relate principal stresses and strains to energy balance:

$$\frac{E_{in}}{E_{out}} = \frac{\sigma_1 \delta\varepsilon_1}{-2\sigma_3 \delta\varepsilon_3} = N \quad \text{“Triaxial”} \tag{2-58}$$

$$\frac{E_{in}}{E_{out}} = \frac{\sigma_1 \delta\varepsilon_1}{-\sigma_3 \delta\varepsilon_3} = N \quad \text{“Bi-axial”} \tag{2-59}$$

E_{in} and E_{out} represent the energy introduced to and the energy released from a soil mass. Eq. 2-59 can be rearranged as:

$$\frac{\sigma_1}{\sigma_3} = -N\frac{\delta\varepsilon_3}{\delta\varepsilon_1} \tag{2-60}$$

For any point along the failure or yield envelope in t-s space:

$$\eta = \frac{t}{s} = \frac{\sigma_1/\sigma_3 - 1}{\sigma_1/\sigma_3 + 1} = \frac{N-1}{N+1} \tag{2-61}$$

Combining Eqns. 2-60 and 2-61 results in an expression for the ratio of principal strains:

$$\frac{\delta\varepsilon_1}{\delta\varepsilon_3} = \frac{N(\eta - 1)}{\eta - 1} \tag{2-62}$$

For this analysis, the ultimate failure state is assumed to occur at the critical state, thus the stress ratio at failure N is replaced by the stress ratio for critical state failure N_{cs} in Eq. 2-62. The value of N_{cs} is obtained by using the critical state friction angle ϕ_{cs} in either Eq. 2-32 or Eq. 2-39. When Eq. 2-62 is substituted into Eq. 2-45, Rowe’s flow rule for bi-axial loading becomes:

$$\frac{\delta\varepsilon_v}{\delta\varepsilon_s} = 1 - \frac{2\eta + 2}{N_{cs} + \eta - N_{cs}\eta + 1} \tag{2-63}$$

In assuming that the dilatancy ratio is based upon energy dissipation, the majority of past models have assumed that dilatancy is the result of stresses imposed on the material. However, Collins et al. (2007, 2010) have shown that volume change in soils is a result of two sources. The first source results from stress changes and the second source is purely kinematic. The kinematic source of dilation follows observations made by Reynolds (1885) in which it was observed that individual grains must move over each other during shear. Muhunthan & Sasiharan (2007) recognized that kinematic sources of dilation are due to soil fabric and following along the lines of the critical state methodology, proposed the following form for energy dissipation:

$$s\sqrt{(\delta\varepsilon_v + \alpha\delta\varepsilon_s)^2 + {M_{BX}}^2\delta\varepsilon_s^2} = s\delta\varepsilon_v + t\delta\varepsilon_s \tag{2-64}$$

Where α is a fabric parameter that accounts for the contribution of kinematic dilatancy. Note that when α is equal to zero, the preceding energy dissipation function reduces to that defined for the modified cam-clay model (MCC) (see Appendix D). Rearranging Eq. 2-64 leads to the flow rule:

$$\frac{\delta\varepsilon_v}{\delta\varepsilon_s} = \frac{M_{BX}^2 + \alpha^2 - \eta^2}{2(\eta - \alpha)} \tag{2-65}$$

After running a series of triaxial tests on Ottawa sand, an empirical relation was developed in which α becomes a function of shear strain, mean stress and void ratio:

$$\alpha = \alpha_m(1 - \exp(-\ell\varepsilon_s))\{\exp(-d_2\langle v_k - v_{k0}\rangle)\} \tag{2-66}$$

$$\alpha_m = B\exp(-bv_{k0}) \tag{2-67}$$

$$v_{k0} = v_0 + \lambda\ln p_c \tag{2-68}$$

$$v_k = v + \lambda\ln p \tag{2-69}$$

B, b, ℓ and d_2 are material constants that must be determined from testing. B and b were found to be 30405 and 16.44 respectively for Ottawa sand. The variable p_c represents the consolidation pressure or initial mean stress and v_{k_0} is the initial specific volume of the sample.

Plots of the flow rule developed by Muhunthan & Sasiharan (2007) can be seen in Figure 2-12 for varying states of anisotropy.

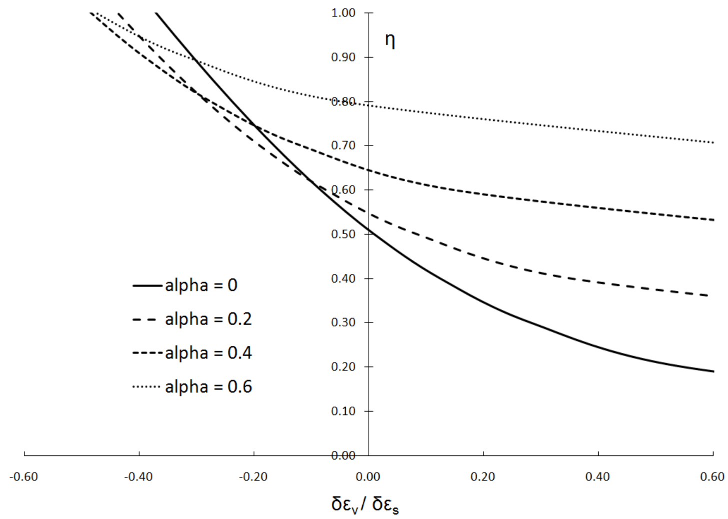

Figure 2-12: Theoretical dilation using Muhunthan & Sasiharan (2007) with varying α.

Due to limited information about the material parameters ℓ and d_2, a simplified form of Eq. 2-66 was used for this study.

$$\alpha = \alpha_m[1 - \exp(-\varepsilon_s)] \tag{2-70}$$

Table 2-1 provides a summary of the different flow rules used in this study. To see detailed derivations for each of the aforementioned flow rules, see Appendices B, C and D. The first three flow rules in Table 2-1 are plotted in Figure 2-13. It can be seen that divergence occurs for high and low values of η.

Table 2-1. Flow rules chosen for analysis.

Rowe (1962)	$\frac{\delta\varepsilon_v}{\delta\varepsilon_s} = 1 - \frac{2\eta + 2}{N_{cs} + \eta - N_{cs}\eta + 1}$
Original Cam-clay (OCC)	$\frac{\delta\varepsilon_v}{\delta\varepsilon_s} = M_{BX} - \eta$
Modified Cam-clay (MCC)	$\frac{\delta\varepsilon_v}{\delta\varepsilon_s} = \frac{M_{BX} - \eta}{2\eta}$
Muhunthan & Sasiharan (2007)	$\frac{\delta\varepsilon_v}{\delta\varepsilon_s} = \frac{M_{BX}^2 + \alpha^2 - \eta^2}{2(\eta - \alpha)}$

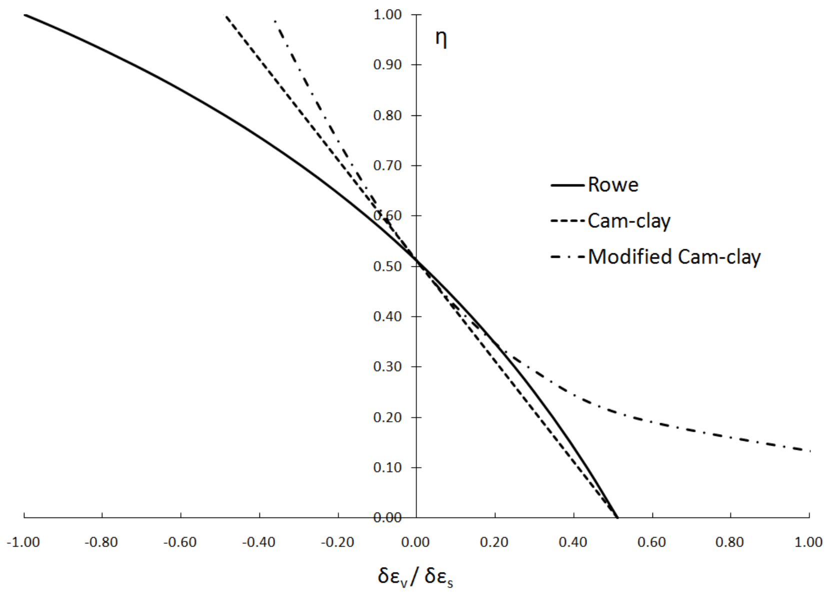

Figure 2-13: Variation in theoretical dilation.

This study will implement the aforementioned flow rules in the cavity expansion analysis proposed next.

CHAPTER THREE

CAVITY EXPANSION IN SANDS

3.1 Cavity Expansion Problem

A schematic of the basic cavity expansion problem for a hollow cylinder or sphere in a continuum is shown in Figure 3-1. The initial stress conditions before cavity expansion are represented as σ_{r_0}. As the cavity expands, the radial stresses acting along the walls of the cavity are at some value σ_r which must be greater than or equal to σ_{r_0}. If the cavity is assumed to expand within an infinite medium, σ_{r_0} theoretically acts at a large radius r equal to infinity.

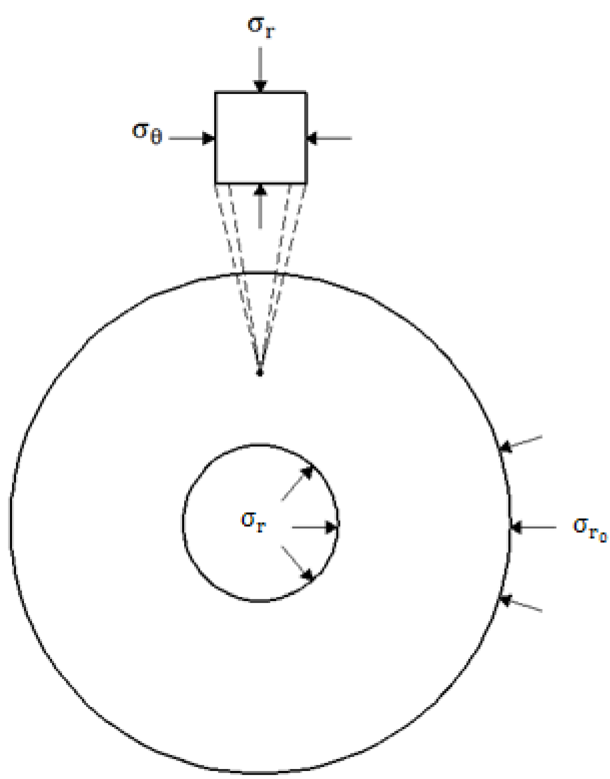

Figure 3-1: Cavity expansion diagram.

The radial and hoop stresses at any point at a radius r from the origin within a medium experiencing cavity expansion are denoted by σ_r and σ_θ, respectively. The stress equilibrium equation is given by (Carter et al. 1986):

$$r\frac{d\sigma_r}{dr} + k(\sigma_r - \sigma_\theta) = 0 \tag{3-1}$$

The variable k in Eq. 3-1 takes a value of 1 for cylindrical cavity expansion and 2 for spherical cavity expansion. The radial and hoop strains (ε_r and ε_θ) induced by cylindrical of spherical expansion are represented by:

$$\varepsilon_r = -\frac{du}{dr} \tag{3-2}$$

$$\varepsilon_\theta = -\frac{u}{r} \tag{3-3}$$

The displacement u can be eliminated by combining Eqns. 3-2 and 3-3 from which the strain compatibility equation is obtained:

$$\varepsilon_r = \frac{d}{dr}(r\varepsilon_\theta) \tag{3-4}$$

Given the equilibrium and compatibility set of equations (Eqns. 3-1 and 3-4), it becomes necessary to define a set of constitutive relations in order to relate stresses and strains. For a linear elastic material, Hooke's law provides a constitutive set of equations which uses properties such as the Poisson's ratio ν and the Young's modulus E.

$$\varepsilon_r = \frac{1}{E}[\sigma_r - \nu(\sigma_z + \sigma_\theta)] \tag{3-5}$$

$$\varepsilon_z = \frac{1}{E}[\sigma_z - \nu(\sigma_r + \sigma_\theta)] \tag{3-6}$$

$$\varepsilon_\theta = \frac{1}{E}[\sigma_\theta - \nu(\sigma_r + \sigma_z)] \tag{3-7}$$

The stress variable σ_z in Eqns. 3-5 through 3-7 is the vertical stress at a depth z below the ground surface. For the situation displayed in Figure 3-1, σ_z acts out of the page. Shear stress τ and strain γ within an element can be calculated using the following relations:

$$\tau = \frac{\sigma_r - \sigma_\theta}{2} \tag{3-8}$$

$$\gamma = \varepsilon_r - \varepsilon_\theta \tag{3-9}$$

Due to the influence of the expanding cavity within the soil medium, various zones form around the cavity as shown in Figure 3-2. The boundary that separates the elastic and plastic regimes is termed the elastic-plastic interface. The elastic-plastic interface is located at some radius R from the center of the cavity. If the cavity increases in size, so too will the value of R.

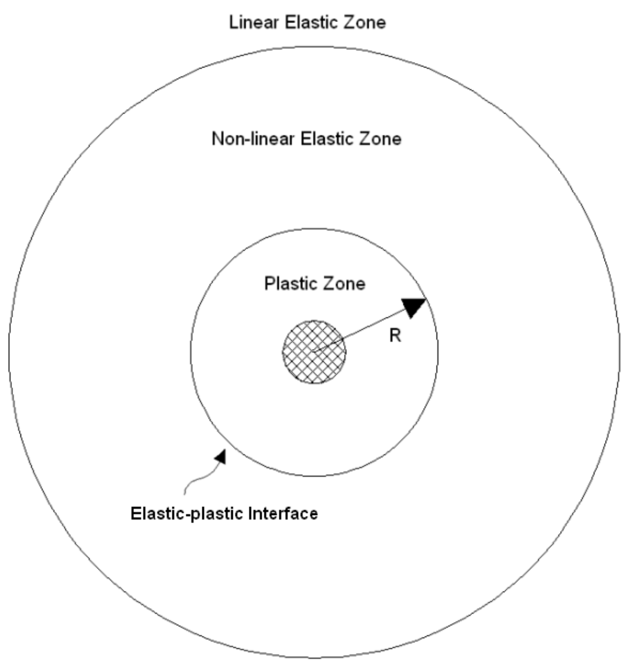

Figure 3-2: Zones in cavity expansion process.

It is important to note that the elastic behavior is divided into a non-linear and a linear elastic region as shown. This is to account for the difficulty often encountered in distinguishing between a truly elastic and truly plastic stress-strain behavior observed in soils. The non-linear elastic behavior is the result of a combination of elastic and plastic behavior (Salgado & Prezzi 2007).

For elements within either of the elastic zones ($r > R$), volumetric strains are taken to be zero throughout which implies that the void ratio will remain constant.

Plastic volumetric strains become present as a result of dilatancy (see Section 2.5) for elements within the plastic zone ($r < R$).

3.2 Outline of Numerical Analysis

A finite difference solution was employed to analyze cylindrical cavity expansion ($k = 1$) in sand assuming an infinitely continuous medium. The solution simulates the creation of cylindrical cavity starting from an initial radius of zero which is analogous to the intrusion of a full displacement pressuremeter or a driven pile into a soil mass. The initial mean stress at any depth of interest is given by:

$$p_0 = \frac{\sigma_v}{3}(1 + 2K_0) \quad (3\text{-}10)$$

K_0 in Eq. 3-10 represents the coefficient of lateral earth pressure.

The plastic zone was broken into incremental shells with equal widths and iterations were carried inward, shell by shell, beginning from the elastic-plastic interface at a radius R where the boundary conditions are known until the cavity wall was reached. This procedure is similar to that adopted by Salgado and his colleagues (1997, 2001, 2003). The radial stress computed at the cavity wall will be equivalent to the limit pressure p_L imposed by a device on the soil mass. The cavity radius, a, is an unknown a priori before executing the analysis. The elastic-plastic radius R is assumed to be any positive value greater than zero. The limit pressure and its associated nuances are described in more detail in the next section.

3.3 The Limit Pressure

The algorithm presented in this study assumed cavity expansion from an initial radius of zero in which the cavity pressure remains constant and is equivalent to p_L from the outset of the expansion process. Thus the analysis proposed in this study is appropriate to simulate displacement type pressuremeter tests (see Appendix A). Figure 3-3 shows test data performed in clay using a displacement type pressuremeter and it can be seen that the cavity pressure does in fact remain fairly constant which supports the constant assumption for the limit pressure. Following Carter et al. (1986), it is postulated that once the limit pressure p_L is reached, the ratio of the elastic-plastic radius, R, to the cavity radius, a, remains constant with further expansion of the cavity. This can be mathematically represented as:

$$\frac{dR}{da} = \frac{R}{a} = \text{constant} \tag{3-11}$$

This implies that the ratio R/a remains constant throughout the entire analysis. Thus, any assumed value for R taken to be greater than zero will be sufficient to solve for the limit pressure p_L.

Note that the radius of the cavity, a, was an unknown before the analysis was initiated. Therefore, it was important to define a termination criterion which could indicate whether or not shell iterations have reached the cavity wall.

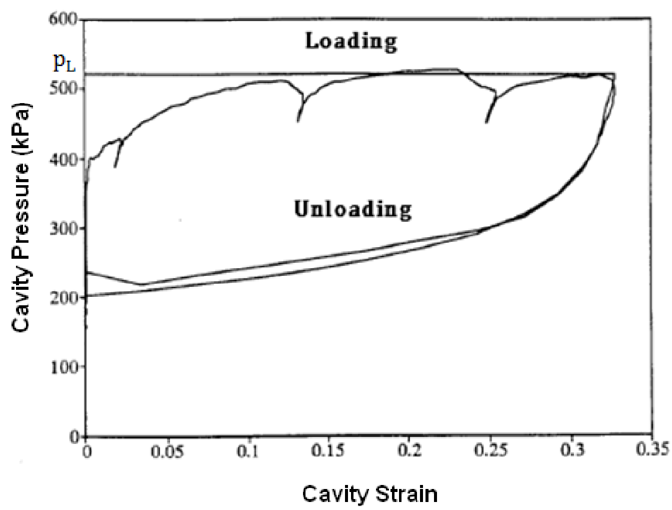

Figure 3-3: Displacement pressuremeter plot (modified after Houlsby & Carter 1993). *This figure displays actual data with a corresponding idealized curve.

A simple termination criterion was implemented in this analysis. Figure 3-4 shows a schematic of the plastic zone after a cavity has been created. The plastic zone was divided evenly into a series of shells represented by the solid black lines each with some radius r. The dashed lines in Figure 3-4 (a) represent the initial radius of any soil particle lying on the outer adjacent solid lines prior to creation of the cavity. The difference between the initial and final radii is represented by the variable u. Beginning at the elastic-plastic interface, it can be seen that the difference between the corresponding values of r and u is quite significant. For each radius moving inward toward the cavity, it can be seen that values of r and u slowly start to converge until reaching the cavity wall where they are taken to be equivalent (Figure 3-4 (b)). For cavity expansion from an initial radius of zero, this indicates that the cavity wall has been reached and that the iterative process across the plastic zone can be terminated.

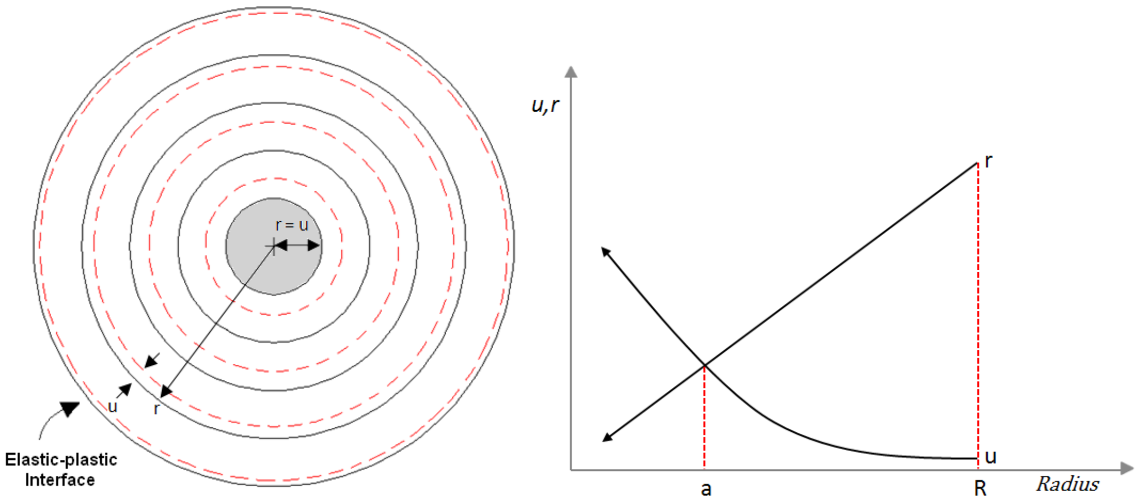

(a) (b)

Figure 3-4: Schematic of plastic zone illustrating the termination condition.

3.4 Stress and Strain Relations for Discrete Shell Analysis in the Plastic Zone

The relation between radial and hoop stresses at failure are related by the stress ratio at failure N (Eq. 2-32 or 2-39):

$$\sigma_r = N\sigma_\theta \tag{3-12}$$

Combining Eqns. 3-1 and 3-12 and then integrating results in the following expression which relates radial stresses at the inner edge (σ_{r_i}) and outer edge (σ_{r_j}) of an incremental shell (Salgado et al. 1997, 2001, 2007):

$$\sigma_{r_i} = \sigma_{r_j}\left(\frac{r_j}{r_i}\right)^{\frac{N-1}{N}} \tag{3-13}$$

The variables r_i and r_j in Eq. 3-13 represent the radii at the inner and outer edges of an incremental shell and N is assumed to represent conditions at the center of the shell. It is necessary to recognize that Eq. 3-13 treats N as a constant across each shell which is indicative of perfectly plastic shear behavior. Only when iterations across each thin incremental shell are carried through using Eq. 3-13 in conjunction with a non-associated flow rule, can strain hardening characteristics of a soil can be captured.

For plane strain conditions, various equations have been presented to express the intermediate stress σ_z. Two such expressions will be used in this study. The first one is obtained using Hooke's law. For plane strain conditions and assuming linear elastic behavior, Hooke's law becomes:

$$\varepsilon_z = 0 = \sigma_z - \nu(\sigma_\theta + \sigma_r) \tag{3-14}$$

Eq. 3-14 can then be rearranged to solve for the intermediate stress σ_z:

$$\sigma_z = \nu(\sigma_\theta + \sigma_r) \tag{3-15}$$

While Hooke's law is sufficient for modeling linear elastic behavior, it is not for plastic soil deformation. Volume changes during plastic deformation will not allow the ratio of axial to lateral strain to remain constant. Thus, Davis (1969) has proposed replacing Poisson's ratio ν with the plastic strain ratio μ in order to better capture plastic soil deformation.

$$\mu = \frac{1}{2}(1 + \sin\phi\sin\psi) \tag{3-16}$$

When Davis' relation μ is used in place of Poisson's ratio ν, σ_z becomes (Salgado et al. 1997, 2001, 2007):

$$\sigma_z = \mu(\sigma_\theta + \sigma_r) \tag{3-17}$$

Substituting Eqns. 3-12 and 3-17 into the general expression for mean stress (Eq. 2-1) results in the following expression (Salgado et al. 2001, 2007):

$$p = \frac{1}{3}(1 + \mu)\left(1 + \frac{1}{N}\right)\sigma_r \tag{3-18}$$

The second method for determining the intermediate stress σ_z makes use of Bishop's parameter b. Rearranging Eq. 2-34:

$$\sigma_z = b\sigma_r + \sigma_\theta(1 - b) \tag{3-19}$$

Substituting Eqns. 3-12 and 3-19 into the general expression for mean stress (Eq. 2-1) results in:

$$p = \frac{1}{3}\left[1 + \frac{2}{N} + b\left(1 - \frac{1}{N}\right)\right]\sigma_r \tag{3-20}$$

The b parameter used above is calculated using Eq. 2-40 which was derived using the SMP failure criterion, thus Eq. 3-20 was only used in this analysis when SMP type failure was assumed.

The preceding relations are dependent on the stress ratio at failure N, which in turn is a function of the internal friction angle ø. As discussed in Section 2.3, test data for soils has shown that the internal friction and dilation angles are related. Recognizing this, past investigators (Salgado et al. 1997, Hao et al. 2010) have used the empirical models of Bolton (1986) (Eq. 2-28) and that of Been & Jefferies (1985) (Eq. 2-25) to control the variations in ø for a soil undergoing plastic shear deformation. This study implements the third relation based on v_λ to track variations in ø for plastic loading (Eq. 2-29). In addition to the preceding empirical relations, Bolton (1986) also proposed the following generalization between the dilation angle ψ, critical state friction angle $ø_{cs}$ and friction angle ø:

$$\psi = 1.25(ø - ø_{cs}) \tag{3-21}$$

For cavity expansion problems in soils, large strains can be expected in the vicinity of the cavity wall. In order to account for this, the radial and hoop strains previously defined (Eqns. 3-2 and 3-3) were redefined in terms of natural strains:

$$\varepsilon_r = -\ln\left[\frac{d_r}{d_{r_0}}\right] = -\ln\left[\frac{r_j - r_i}{(r_j - u_j) - (r_i - u_i)}\right] \tag{3-22}$$

$$\varepsilon_{\theta} = -\ln\left[\frac{r_i}{r_i - u_i}\right] \tag{3-23}$$

$$\varepsilon_{v} = -\ln\left[\frac{r_j^2 - r_i^2}{\left(r_j - u_j\right)^2 - (r_i - u_i)^2}\right] \tag{3-24}$$

The negative sign convention in the preceding relations is consistent with contraction being assumed positive. Again, the subscripts i and j are used in Eqns. 3-22 through 3-24 to denote values at the inner and outer edges of each incremental shell as shown in Figure 3-5. As discussed in Section 3.3, u_i steadily increases when movement is made inward from the elastic-plastic interface.

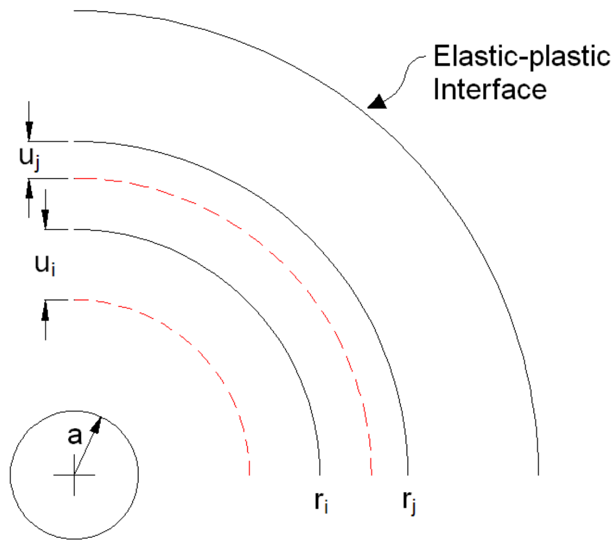

Figure 3-5: Inner and outer radii and displacements for a single incremental shell.

Plastic deformation within each incremental shell was described using the discretized form of the flow rule as:

$$\frac{\delta\varepsilon_v}{\delta\varepsilon_s} = \frac{\varepsilon_{v_j} - \varepsilon_{v_i}}{\left(\varepsilon_{r_j} - \varepsilon_{r_i}\right) - \left(\varepsilon_{\theta_j} - \varepsilon_{\theta_i}\right)} \tag{3-25}$$

As detailed before (Section 2.5), four different flow rules are used here to study their effects on the analysis. The flow rules in Table (2-1) are re-expressed as:

Rowe (1962): $$d = -\frac{\delta\varepsilon_v}{\delta\varepsilon_s} = \frac{2\eta + 2}{N_{cs} + \eta - N_{cs}\eta + 1} - 1 \quad (3\text{-}26)$$

Cam-Clay: $$d = -\frac{\delta\varepsilon_v}{\delta\varepsilon_s} = -(M_{BX} - \eta) \quad (3\text{-}27)$$

Modified Cam-Clay: $$d = -\frac{\delta\varepsilon_v}{\delta\varepsilon_s} = -\frac{{M_{BX}}^2 - \eta^2}{2\eta} \quad (3\text{-}28)$$

Muhunthan & Sasiharan (2007): $$d = -\frac{\delta\varepsilon_v}{\delta\varepsilon_s} = -\frac{{M_{BX}}^2 + \alpha^2 - \eta^2}{2(\eta - \alpha)} \quad (3\text{-}29)$$

Note that the negative sign used in Eqns. 3-26 through 3-29 arises because the dilatancy expressions in Section 2.4 were derived assuming that dilation was positive, whereas the sign convention adopted in the numerical analysis treats contraction as being positive. Substituting Eqns. 3-22 through 3-24 into 3-25 results in the following equation:

$$\varepsilon_{v_j} + d\left(\varepsilon_{r_j} - \varepsilon_{\theta_j}\right) = \ln\left[\frac{F_1(u_i)F_2(u_i)}{F_3(u_i)}\right] \quad (3\text{-}30)$$

where

$$F_1(u_i) = \frac{\left(r_j - u_j\right)^2 - (r_i - u_i)^2}{r_j^2 - r_i^2} \quad (3\text{-}31)$$

$$F_2(u_i) = \left[1 + \frac{u_i - u_j}{r_j - r_i}\right]^d \quad (3\text{-}32)$$

$$F_3(u_i) = \left[1 - \frac{u_i}{r_i}\right]^d \quad (3\text{-}33)$$

Solution of Eq. 3-30 allows known values at the outer edge of an incremental ring to be utilized in order to solve for the unknown, u_i, at the inner edge. Since Eq. 3-30 is an implicit function, u_i needs to be solved using either the Newton-Raphson algorithm or unconstrained non-linear optimization. It should also be noted that the left side of Eq. 3-30 represents known variables at the outer edge of an incremental ring.

3.5 Boundary Conditions at Elastic-Plastic Interface

Before the finite difference algorithm could be initiated, boundary conditions needed to be defined at the elastic-plastic radius. This required satisfying stress and strain compatibility between the elastic and plastic regimes. The radial and hoop stresses (σ_R, σ_T) and strains (ε_R, ε_T) at the elastic-plastic interface were then determined using the following stress and strain relations (Salgado et al. 1997, 2001, 2007):

$$\sigma_R = \frac{2Np_0}{N+1} \tag{3-34}$$

$$\sigma_T = \frac{\sigma_R}{N} \tag{3-35}$$

$$\varepsilon_R = \frac{N-1}{N+1}\frac{p_0}{2G} = -\varepsilon_T \tag{3-36}$$

The radial strain ε_R and hoop strain ε_T at the elastic-plastic interface are parameterized by the linear shear modulus G. Since non-linear elastic behavior is assumed adjacent to the plastic zone, G at the elastic-plastic interface is a reduced value of the linear elastic shear modulus G_0 as shown in Figure 3-6.

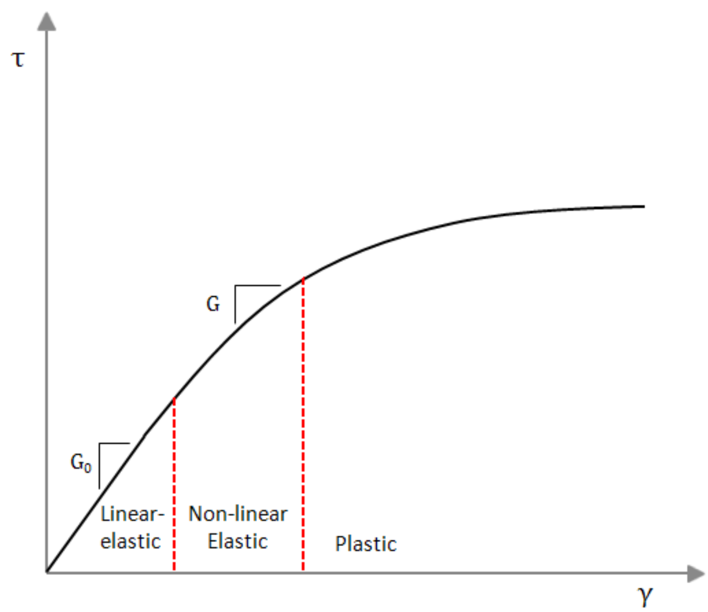

Figure 3-6: Variations in shear modulus.

Hardin & Black (1968) proposed an empirical relation from which G_0 can be attained:

$$G_0 = p_a c_g \frac{(e_g - e)^2}{1 + e} \left({}^{p}/_{p_a}\right)^{n_g} \tag{3-37}$$

The empirical constants c_g, e_g, n_g in equation 3-37 vary depending on sand type and p_a is atmospheric pressure (100 kPa). Using the non-linear degradation model developed by Ishibashi & Zhang (1993), the value of G is obtained at the elastic-plastic interface after some iteration.

$$G = G_0 K p^n \tag{3-38}$$

$$K = 0.5\left\{1 + \tanh\left[\ln\left(\left(\frac{0.000102}{\gamma}\right)^{0.492}\right)\right]\right\} \tag{3-39}$$

$$n = 0.272\left\{1 - \tanh\left[\ln\left(\left(\frac{0.000556}{\gamma}\right)^{0.4}\right)\right]\right\} \tag{3-40}$$

$$\gamma = \frac{\tau}{G} \tag{3-41}$$

In the procedure outlined by Salgado & Prezzi (2007), the non-linear elastic zone was subdivided into a series of shells and iterations were carried through to obtain an equivalent linear value of the shear modulus using equations for an elastic hollow cylinder of infinite radius. This analysis used a simpler approach which involved iterating at one location, the elastic-plastic radius, to obtain a compatible value for the shear modulus. Figure 3-7 shows variations for different parameters in the cavity expansion problem. The shear modulus decreases across the non-linear elastic zone from the initial small strain shear modulus G_0 until reaching the elastic plastic radius where it assumes a reduced value G. Across the plastic zone, it can be seen that the friction angle initially assumes a peak value ϕ_{peak} at the elastic-plastic radius and decreases towards the critical state value ϕ_{cs} at the cavity wall. Conversely, the radial stress increases from the value at the elastic-plastic radius σ_R until reaching the cavity wall where it is taken to be the limit pressure p_L.

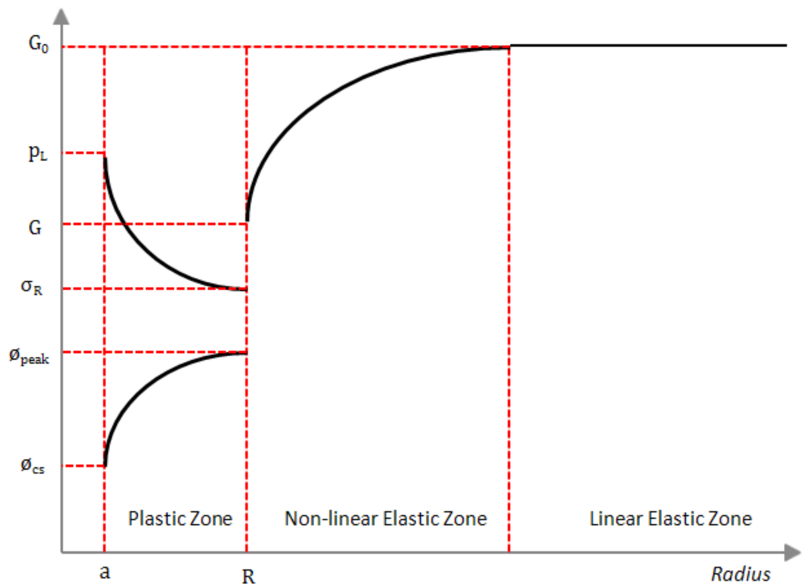

Figure 3-7: Parameter changes across associated zones
(modified after Salgado & Prezzi 2007).

3.6 Flow Chart for Cavity Expansion Algorithm

The flow charts shown in Figures 3-8 through 3-10 display each sequence of the cylindrical cavity expansion algorithm. The algorithm consisted of three distinct iterative segments. The finite difference segment that was used within the plastic zone involved the repetition of the same iterative process several times over a series of incremental shells.

The first iteration segment in the algorithm was necessary to obtain compatible values for the radial stress σ_R, hoop stress σ_T and peak friction angle $ø_{peak}$ at the elastic-plastic interface. In order to accomplish this, the boundary condition expressions described in Section 3.5 were used in combination with expressions for a failure criterion and friction angle model. Once compatible values of σ_R, σ_T, and $ø_{peak}$ were obtained, a second iterative approach was initiated to calculate the representative strains and displacements.

In order to calculate representative values of strain and displacement at the elastic-plastic interface, a compatible value of the non-linear shear modulus G needed to be calculated which captured the displacements across the elastic zones. Therefore, a second iterative segment that used previously calculated values of σ_R and σ_T was used to compute a compatible value for G. These iterations required using the empirical relations of Hardin & Black (1968) followed by that of Ishibashi & Zhang (1993).

The preceding iterative calculations were carried out to solve for the boundary conditions at the elastic-plastic interface. From these boundary conditions, finite difference calculations were initiated across the plastic zone starting from the shell adjacent to the elastic-plastic interface. Each shell required an iterative process to obtain compatible values of stress, strain and the mobilized friction angle before the analysis could shift inward to the next adjacent shell. The iterative process was terminated when the cavity wall was reached where the radial stress acting on the inside of the incremental shell σ_{r_i} was taken to be equivalent to the limit pressure p_L.

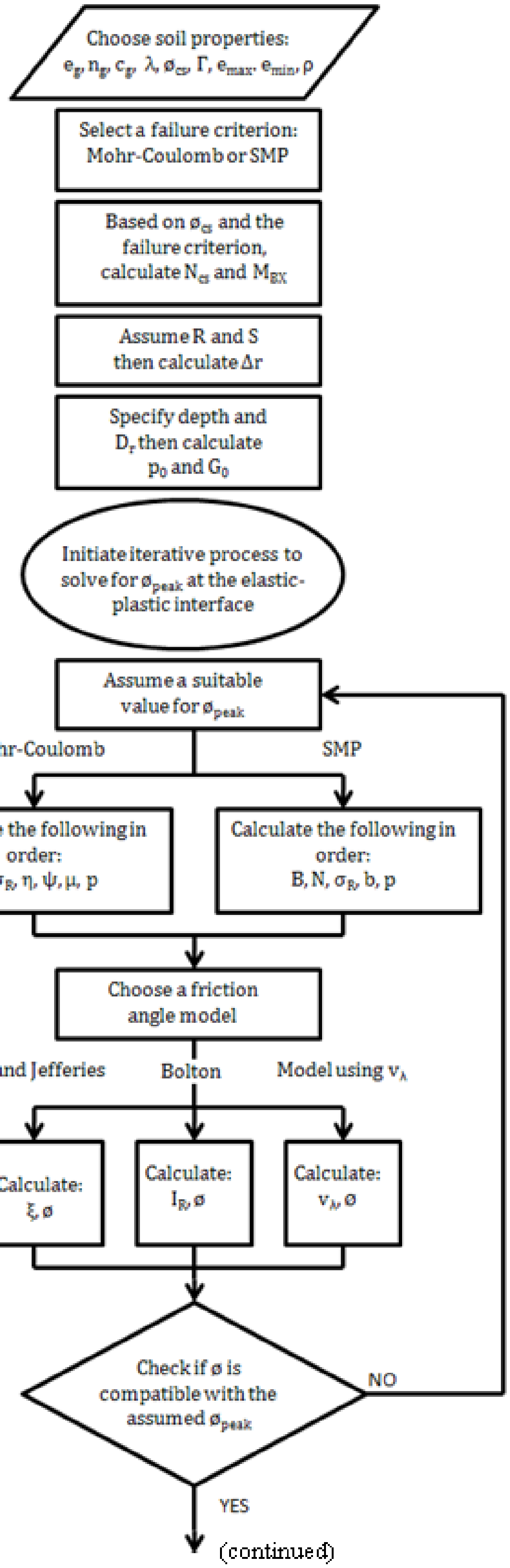

Figure 3-8: Flow chart showing iteration segment to obtain σ_R, σ_T and $ø_{peak}$.

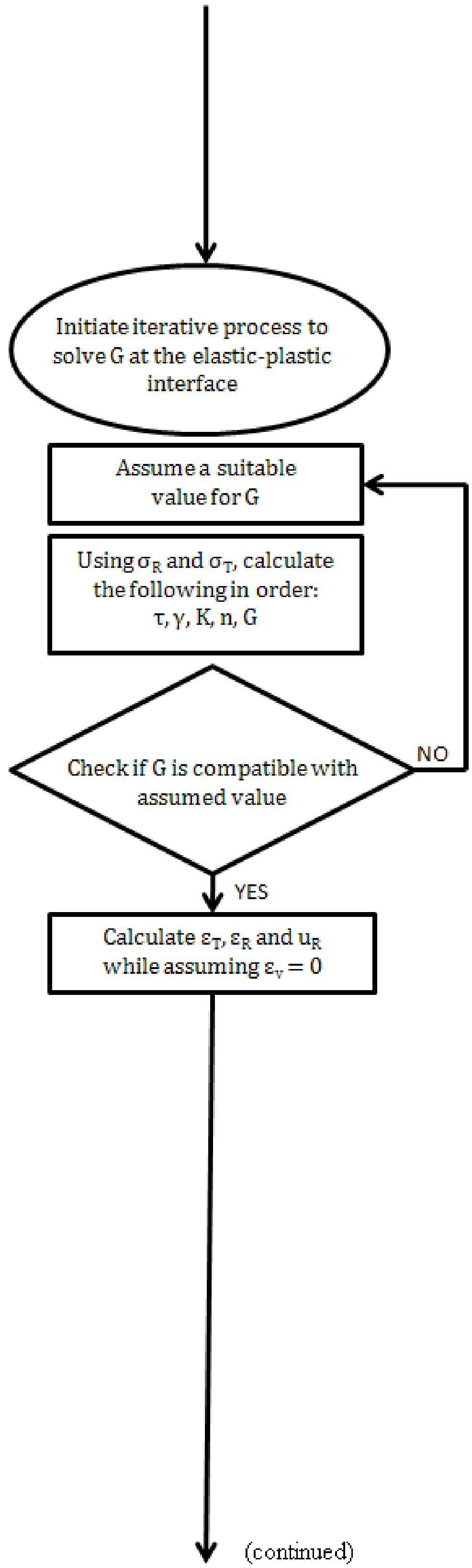

Figure 3-9: Flow chart showing iteration segment to obtain G, ε_R and ε_T.

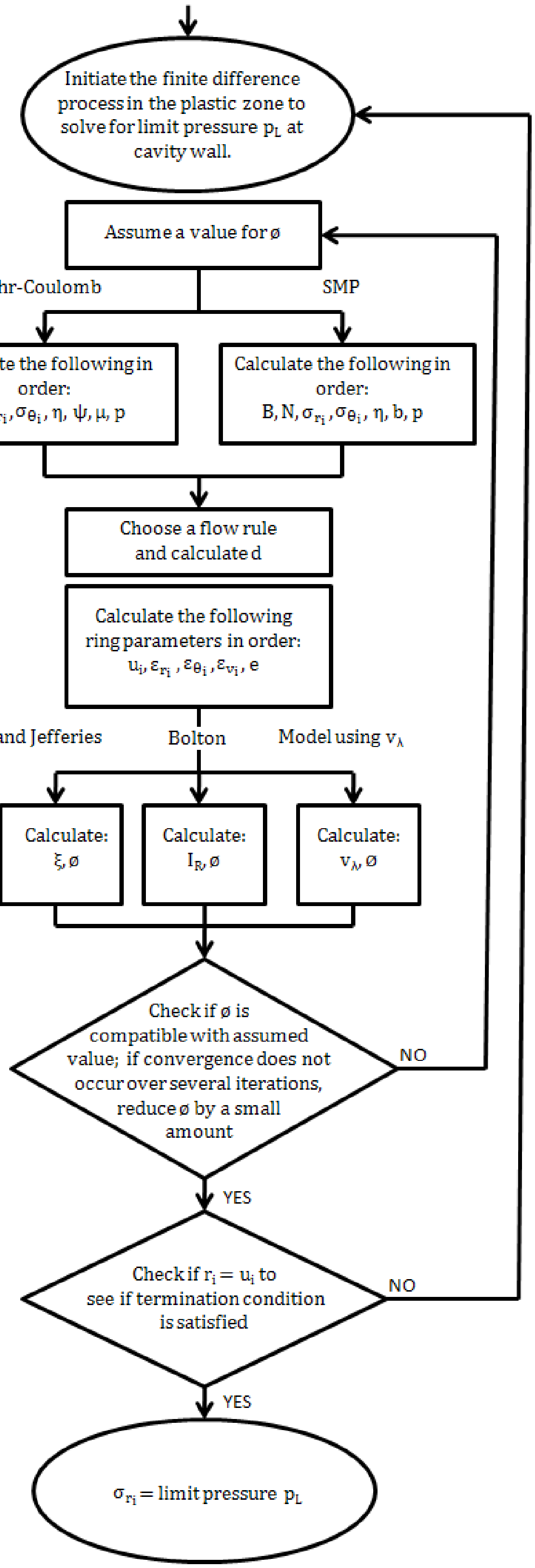

Figure 3-10: Flow chart showing iteration segment across plastic zone.

3.7 Step-by-Step Progress through the Cavity Expansion Algorithm

This section details each of the calculations shown in the preceding flow chart for the cylindrical cavity expansion analysis.

Iterative Approach for Calculations of Stresses and Strains at Elastic-plastic Interface:

- Specify material properties for the sand to be modeled.
- Choose a failure criterion; Mohr-Coulomb or SMP to obtain a representative value for M_{BX}:

  <u>Mohr-Coulomb:</u>

  - Calculate N_{cs} (2-32) using $\o_{cs}$.
  - Calculate M_{BX} (2-16).

  <u>SMP:</u>

  - Calculate N_{cs} (2-39) using $\o_{cs}$.
  - Calculate M_{BX} (2-61).
- Specify R and the number of incremental shells S that will subdivide the plastic regime. The width Δr of each shell is simply:

$$\Delta r = \frac{R}{S} \tag{3-42}$$

  Following Salgado & Prezzi (2007), it is suggested to subdivide the plastic zone into 1,000 to 2,000 sections.
- Specify depth and in-situ relative density for analysis.
- Calculate p_0 (3-10) and G_0 (3-37).
- Iterate to obtain $\o_{peak}$ at the elastic-plastic interface following these steps:

  1. Assume a value for $\o_{peak}$ then depending on the failure criterion:

     <u>Mohr-Coulomb:</u>

     - Calculate N (2-32).
     - Calculate σ_R (3-34).
     - Calculate η (2-61).

- Calculate ψ (3-21).
- Calculate μ (3-16).
- Calculate p (3-18) with $\sigma_r = \sigma_R$.

<u>SMP:</u>

- Calculate B (2-33).
- Calculate N (2-39).
- Calculate σ_R (3-34).
- Calculate b (2-40).
- Calculate p (3-20) with $\sigma_r = \sigma_R$.

2. Choose an empirical model to obtain the peak friction angle $ø_{peak}$:

   <u>Bolton (1986):</u>

   - Calculate I_R (2-26).
   - Calculate a new $ø_{peak}$ (2-28).

   <u>Been & Jefferies (1985):</u>

   - Calculate ξ (2-22).
   - Calculate a new $ø_{peak}$ (2-25).

   <u>New model using v_λ:</u>

   - Calculate v_λ (2-21).
   - Calculate a new $ø_{peak}$ (2-29).

3. Iterate from step 1 until the difference between the new value of $ø_{peak}$ and the assumed value are satisfactorily small.

- Iterate to ensure a compatible shear modulus at the elastic-plastic interface:
  1. Assume a value for G.
  2. Calculate σ_T (3-35) from σ_R.
  3. Calculate τ (3-8) using σ_R and σ_T.
  4. Calculate γ (3-41).
  5. Calculate G (3-38).
  6. Iterate from step 2 until G converges.
- From the non-linear shear modulus G computed at the elastic-plastic interface, obtain ε_T and ε_R (3-36).

- Assuming that the strains near the non-linear elastic zone are sufficiently small, the displacement u_R at the elastic-plastic interface is computed as:

$$u_R = \varepsilon_R R \tag{3-43}$$

The volumetric strain ε_v at the elastic plastic interface is taken to be zero.

Limit Pressure at the Cavity Wall Using Shell by Shell Calculations:

The stresses, strains and displacements previously solved can now be thought of as known values at the outer side of the first incremental shell that borders the elastic-plastic interface within the plastic zone. Therefore these values will now be denoted with the subscript "j".

- Calculate the stresses, strains and displacements per shell using the following process. It should be noted that r_i, r_j, u_j, σ_{r_j}, σ_{θ_j} and e are all known values at this point.
  1. Assume a value for ø which should initially be specified as the value solved for the previous shell then calculate p at the center of the shell based on one of the proposed failure criterion:

     Mohr-Coulomb:

     - Calculate N (2-32).
     - Calculate σ_{r_i} (3-13) and σ_{θ_i} (3-12).
     - Calculate η (2-58).
     - Calculate ψ (3-21).
     - Calculate μ (3-16).
     - Calculate p using:

$$p = \frac{1}{3}(1+\mu)\left(1+\frac{1}{N}\right)\left(\frac{\sigma_{r_i}+\sigma_{r_j}}{2}\right) \tag{3-44}$$

     SMP:

     - Calculate B (2-33).
     - Calculate N (2-39).

- Calculate σ_{r_i} (3-13) and σ_{θ_i} (3-12).
- Calculate b (2-40)
- Calculate p using:

$$p = \frac{1}{3}\left[1 + \frac{2}{N} + b\left(1 - \frac{1}{N}\right)\right]\left(\frac{\sigma_{r_i} + \sigma_{r_j}}{2}\right) \tag{3-45}$$

2. Choose a flow rule and calculate *one* value for d from (3-26) through (3-29). If the flow rule of Muhunthan & Sasiharan (2007) is chosen, the anisotropy parameter α (2-70) must be calculated using the current deviator strain ε_s.

$$\varepsilon_s = \varepsilon_{r_j} + \varepsilon_{\theta_j} \tag{3-46}$$

3. Solve (3-30) for u_i using either the Newton-Raphson algorithm or unconstrained non-linear optimization.
4. Calculate ε_{v_i}, ε_{r_i} and ε_{θ_i} using (3-22) through (3-24).
5. Calculate the new void ratio at the center of the shell using:

$$e = \left[(1 + e_0)\exp\left(-\varepsilon_{v_i}\right)\right] - 1 \tag{3-47}$$

where e_0 is the in-situ void ratio before cavity expansion occurs.

6. Choose an empirical model to track the mobilized friction angle ø:

<u>Bolton (1986):</u>

- Calculate I_R (2-26).
- Calculate a new $ø_{peak}$ (2-28).

<u>Been & Jefferies (1985):</u>

- Calculate ξ (2-22).
- Calculate a new $ø_{peak}$ (2-25).

<u>New model using v_λ:</u>

- Calculate v_λ (2-21).
- Calculate a new $ø_{peak}$ (2-29).

7. Iterate from step 2 until the difference between the value of ø computed in step 6 and the assumed value from step 1 are satisfactorily small.

Note: If values of ø do not converge, decrease the assumed value for ø by a small amount until compatibility is achieved.

- If the difference between r_i and u_i is not satisfactorily small, the cavity wall has not been reached thus the recursive process continues to the next shell so that all values with subscript "i" are initialized to subscript "j".
- If the difference between r_i and u_i is satisfactorily small, use an algorithm such as the bisection method to solve for stresses at the cavity wall. Since equation 3-30 becomes undefined at the cavity wall when u_i is equivalent to r_i, assume that r_i is larger than u_i by a very small amount. Once convergence occurs for the ring bordering the cavity wall, report σ_{r_i} which is analogous to the limit pressure.

3.8 Soil Properties

The algorithm described in this study used empirical and critical state relations, thus material constants and properties needed to be specified as input. The intrinsic material properties chosen for this analysis were representative of typical sands:

Empirical constants for computation of G_0: e_g = 2.17; n_g = 0.44; c_g = 612;

Critical state properties: λ = 0.024; Γ = 1.986; $ø_{cs}$ = 29;

Soil properties: e_{min} = 0.61; e_{max} = 0.90; γ = 20 kPa;

Salgado & Prezzi (2007) suggested that K_0 for sands should range between 0.40 and 0.50 thus an average of 0.45 was implemented.

CHAPTER FOUR

RESULTS AND INTERPRETATION

4.1 Comparisons between Predicted and Measured Limit Pressures

Ghionna et al. (1989) presented data obtained from a series of displacement pressuremeter tests performed in a calibration chamber using Ticino sand. Limit pressure data from 42 pressuremeter tests were compared to predicted limit pressures obtained from the algorithm presented in this study. The data was divided into three groups representing ranges of 0.4-0.6, 0.6-0.8 and 0.8-1.0 for the coefficient of lateral earth pressure K_0. A linear regression analyses between the predicted and measured values of p_L is shown in Figure 4-1. The properties implemented into the algorithm to approximately characterize Ticino sand are displayed in Table 4-1. The friction angle model of Bolton (1986), Rowe's flow rule and the Mohr-Coulomb failure criterion were used in combination for this analysis.

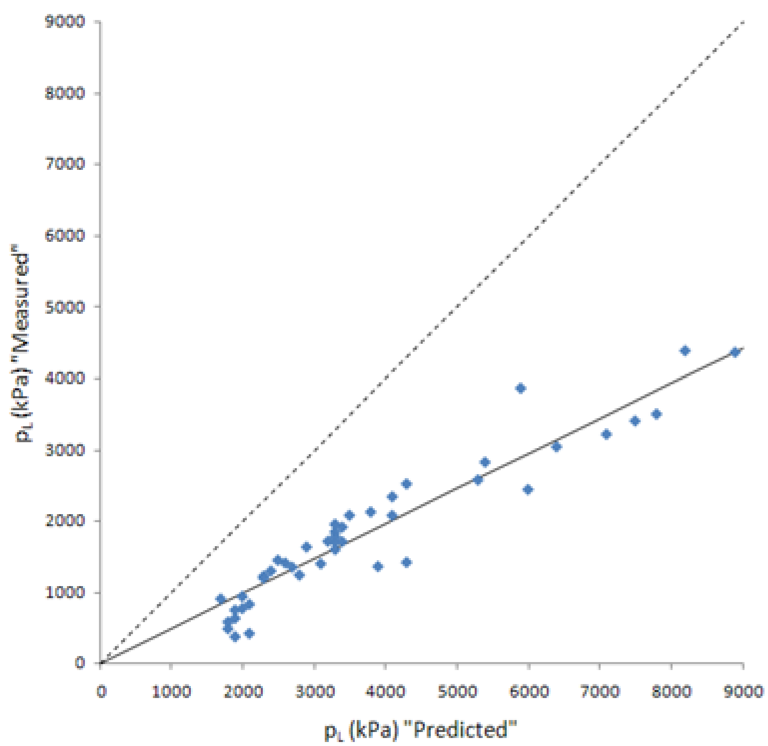

Figure 4-1: Linear regression analysis showing measured versus predicted values of limit pressure p_L.

Table 4-1: Properties assumed for Ticino sand.

e_g	n_g	c_g	λ	Γ	ϕ_{cs}°	e_{min}	e_{max}	γ (kPa)
2.17	0.44	612	0.056	1.975	33	0.60	0.89	10.0

As can be seen from Figure 4-1, measured values of p_L were significantly lower than the predicted values. The over predictive nature of the algorithm presented in this study may be a result of a few factors. The first, and potentially the most significant factor, being that this study neglected the effects of particle crushing. Prior research by Hao et al. (2010) incorporated particle crushing concepts presented by Russell & Khalili (2006) into a cavity expansion model similar to that presented here. Hao and his colleagues observed that predicted values of the limit pressure which assumed particle crushing were approximately 40 percent lower than corresponding predictions that neglected particle crushing.

Past research has also shown that the length to diameter ratio L/D of a pressuremeter strongly influences limit pressure readings. As L/D increases, the plane strain assumption becomes more valid. The displacement pressuremeter employed by Ghionna et al. (1989) had an L/D of 6 which is lower than the value of 10 that is commonly implemented in pressuremeter testing. As such, limit pressures were corrected to represent an L/D of 10. The linear regression analysis presented above implemented the corrected limit pressures which were approximately 17 percent lower than the uncorrected values. The accuracy of the aforementioned corrections is debatable thus there is slight uncertainty in the measured values for limit pressure used in the preceding comparative analysis.

4.2 Comparison between Models

Before performing detailed analyses, a comparison of the results from the current study was done with that proposed by Salgado and his colleagues (Salgado et al. 1997, 2001, 2007). Figure 4-2 shows the variation of the ratio of the non-linear shear modulus G to the small strain shear modulus G_0 at the elastic-plastic interface as a function of D_r and depth obtained from the current model and that by Salgado and his colleagues.

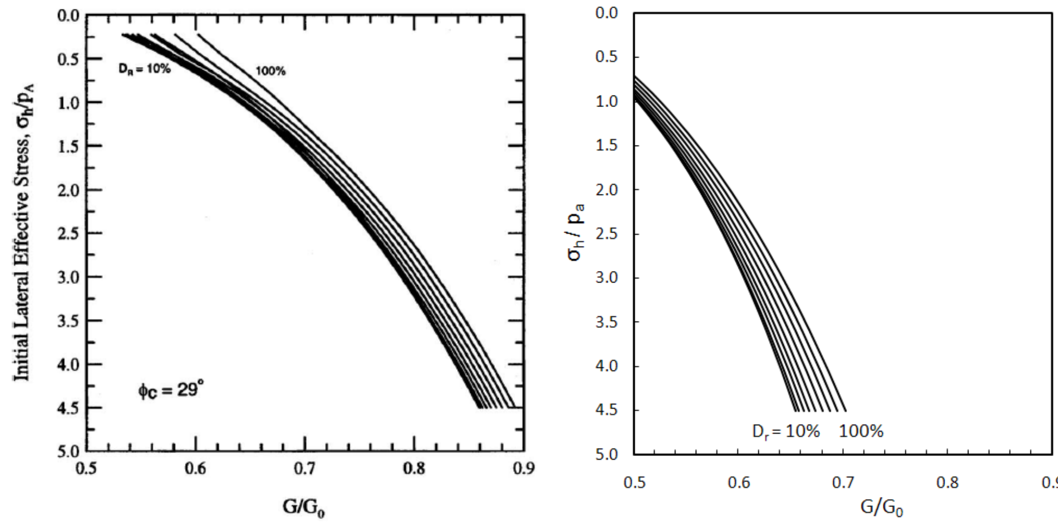

(a) (b)

Figure 4-2: Shear modulus at elastic-plastic interface
(modified after Salgado & Prezzi 2007).
(a) Model presented by Salgado & Prezzi (2007) for $\o_{cs} = 29^{\circ}$
(b) Model presented in this study for $\o_{cs} = 29^{\circ}$

It can be seen that the G/G_0 values from Salgado's analyses are slightly larger at a given depth, which is a result of their using equivalent linear values across the elastic zones. Note that this use of equivalent linear values for G, N and p_L enables them to calculate bearing capacity or cone resistance solutions (Salgado & Randolph 2001), whereas the focus of this study is the pressuremeter.

Figure 4-3 (a) shows the results obtained from the algorithm presented by Salgado which used the combination of Bolton (1986), Rowe (1962) and Mohr-Coulomb for the friction angle model, flow rule and failure criterion respectively. The results shown in Figure 4-3 (b) were obtained from the algorithm presented in this study assuming the same combination. All stresses shown in Figure 4-3 are normalized to atmospheric pressure (p_a = 100 kPa). It can be seen that as the confining stress increases, values for the limit pressure increase. The opposite effect is observed for R/a values with increase in confining stress. This implies that as depth increases, the cavity needs to be expanded to greater radii to achieve the limit pressure.

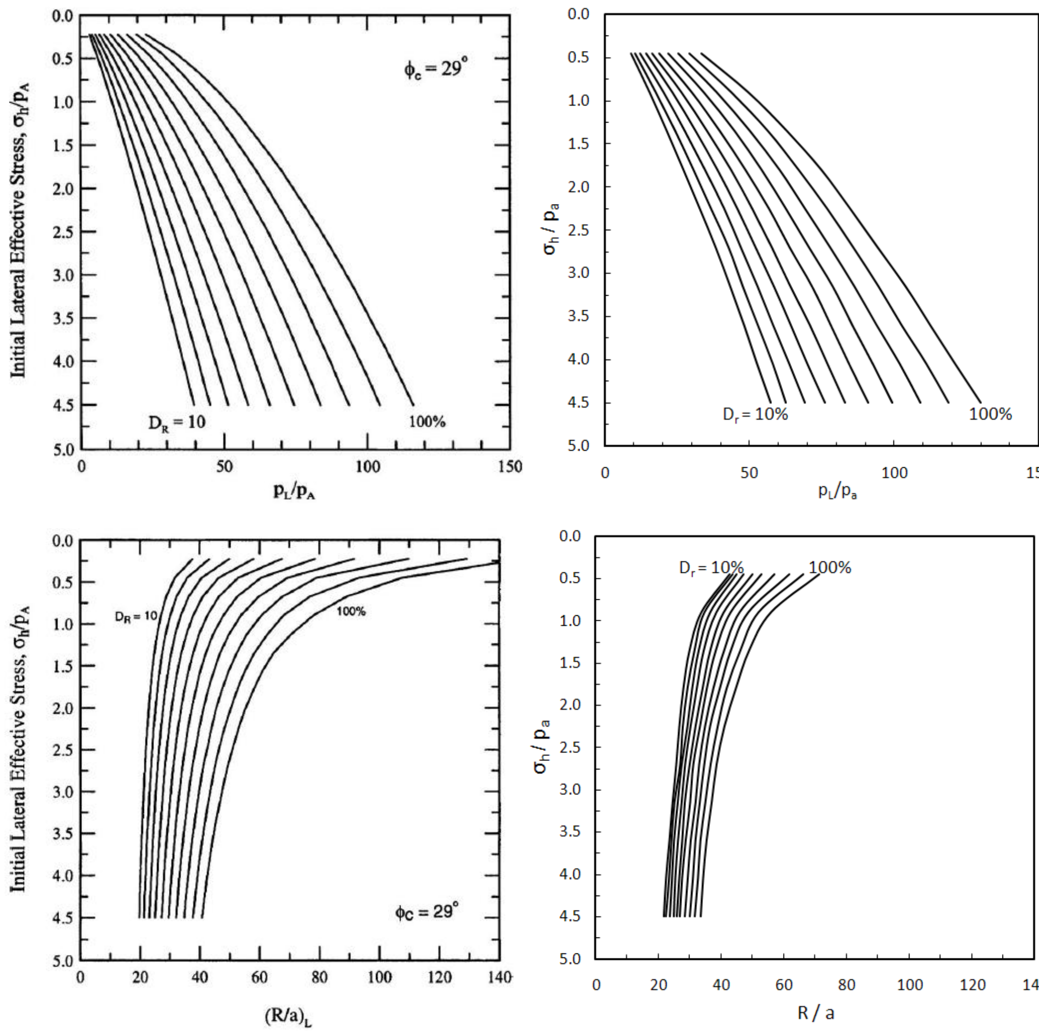

(a) (b)

Figure 4-3: Initial lateral stress versus limit pressure
(modified after Salgado & Prezzi 2007).
(a) Model presented by Salgado & Prezzi (2007) for $ø_{cs}$ = 29°
(b) Model presented in this study for $ø_{cs}$ = 29°

Note that the results shown in Figure 4-3 (a) are for equivalent linear values, whereas, those shown in Figure 4-3 (b), are direct values. However, it can be seen that both models produce very similar results for the limit pressure. The model presented in this study predicts slightly higher values than those from Salgado's model for a given value of relative density. The difference in values for R/a may be the result of us not using an equivalent linear value for G at the elastic-plastic interface and opting to iterate across the plastic zone using flow rules that are expressed such that they are a function of the friction angle ø rather than the dilation angle ψ. For example, Salgado and his colleagues chose to express Rowe's flow rule using:

$$d = \sin\psi \tag{4-1}$$

whereas this study uses Eq. 3-26 which is a function of ø.

4.3 Parametric Study

Several different combinations of the models for flow rule, friction angle and failure criterion were implemented in the numerical analysis to assess their influence on the limit pressure. The following lists the different combinations expressed using the notation:

flow rule : friction angle model : failure criterion

friction angle model =	flow rule =	failure criterion =
B → Bolton (1986)	R → Rowe (1962)	M-C → Mohr-Coulomb
v_λ → Model using v_λ	OCC → Original Cam-clay	SMP → SMP
B&J → Been and Jefferies (1985)	MCC → Modified Cam-clay	
	M → Muhunthan & Sasiharan (2007)	

For example, an analysis using the friction angle model of Bolton (1986), the Modified Cam-clay flow rule and the SMP failure criterion is represented by the combination B : MCC : SMP.

The analyses are performed to a maximum depth of 50 meters in increments of five meters. The study assumes an elastic-plastic radius of 100 meters and subdivides the plastic zone into 2,000 incremental shells.

4.4 Results from Analysis Using v_λ Parameter

When Bolton's model (Eq. 2-25) was replaced by Eq. 2-27 to track changes in the friction angle, the predicted values for limit pressure and R/a increased. Figure 4-4 (a) shows the results for the combination B : R : M-C whereas Figure 4-4 (b) shows those for the combination v_λ : R : M-C.

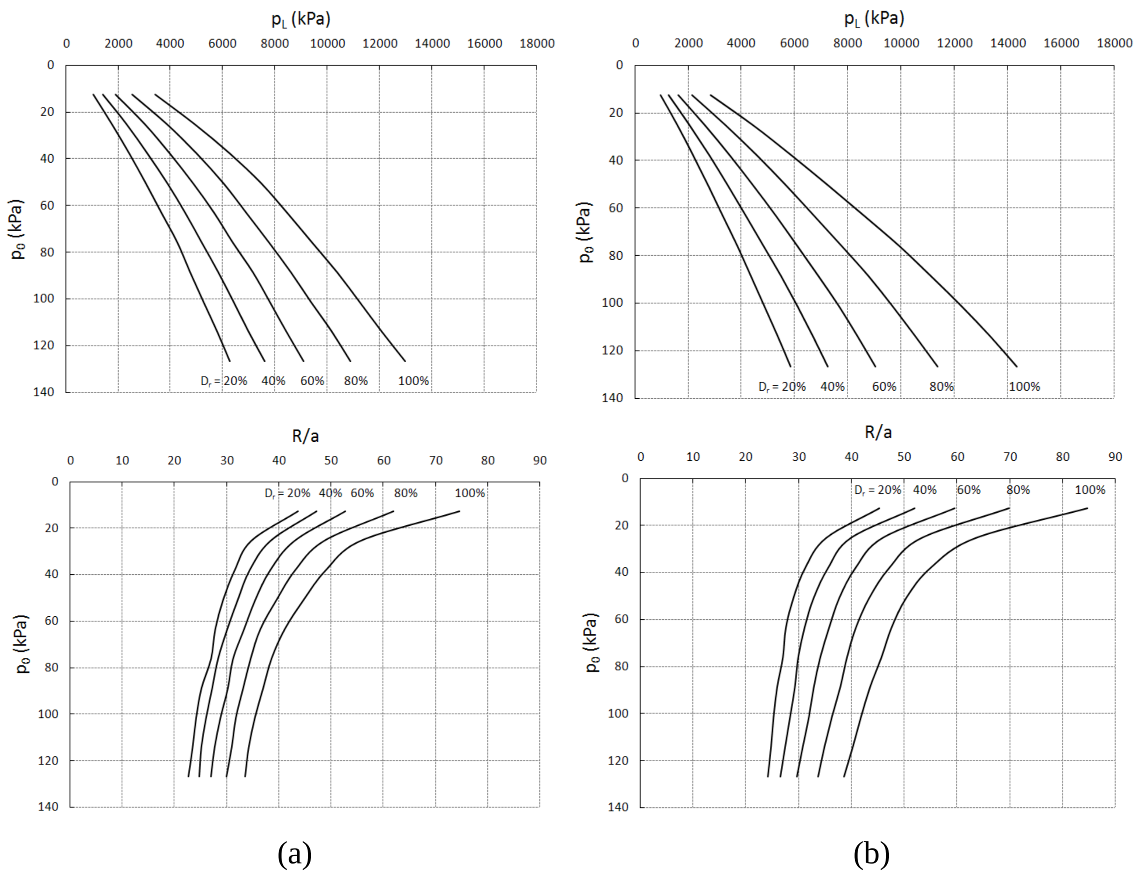

Figure 4-4: Influence of friction angle models on the limit pressure and R/a for $ø_{cs} = 29^{\circ}$.
(a) Combination B : R : M-C
(b) Combination v_λ : R : M-C

It can be seen that the algorithm produces larger values of the limit pressure and R/a when the friction is governed by v_λ rather than Bolton's model. Difficulty was encountered when incorporating the model developed by Been & Jefferies (1985), thus corresponding output was not included in this study.

4.5 Flow Rule and Failure Criterion Combinations

A series of analyses were performed by changing the flow rule model within the cavity expansion algorithm while not varying the friction angle model and failure criterion. It was observed that changing the flow rule had almost no effect on the output as seen in Figure 4-5.

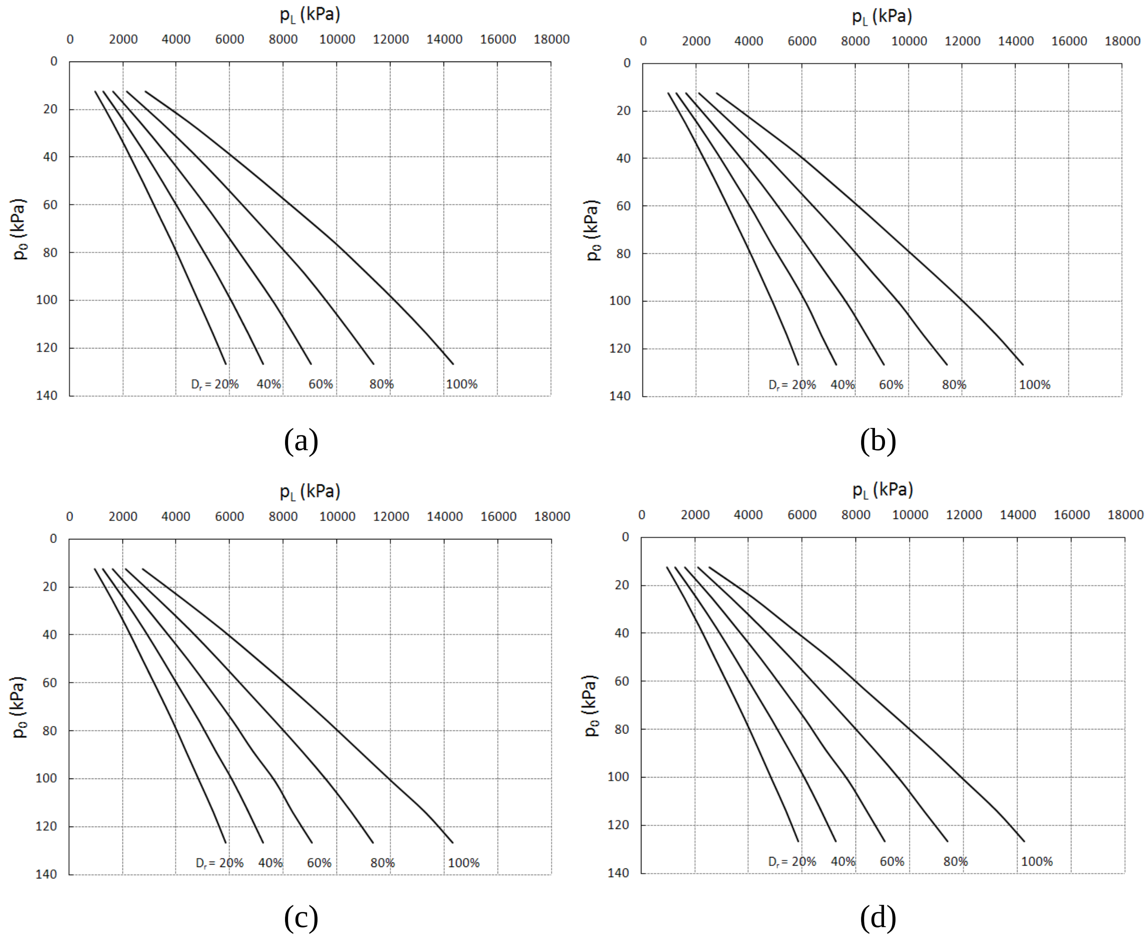

Figure 4-5: Influence of flow rules on the limit pressure for $ø_{cs} = 29^{\circ}$.
(a) v_{λ} : R : M-C (b) v_{λ} : OCC : M-C
(c) v_{λ} : MCC : M-C (d) v_{λ} : M : M-C

Results that were obtained when the Mohr-Coulomb failure criterion was interchanged with the SMP criterion while holding the friction angle model and flow rule constant are shown in Figure 4-6. As the in-situ mean stress increases, it becomes apparent that the SMP failure criterion predicts slightly larger values of limit pressure than that obtained when using the Mohr-Coulomb failure criterion. These results were expected since it was shown in Section 2.4 that strengths predicted by the Mohr-Coulomb criterion tend to be conservative as opposed to those calculated from the SMP.

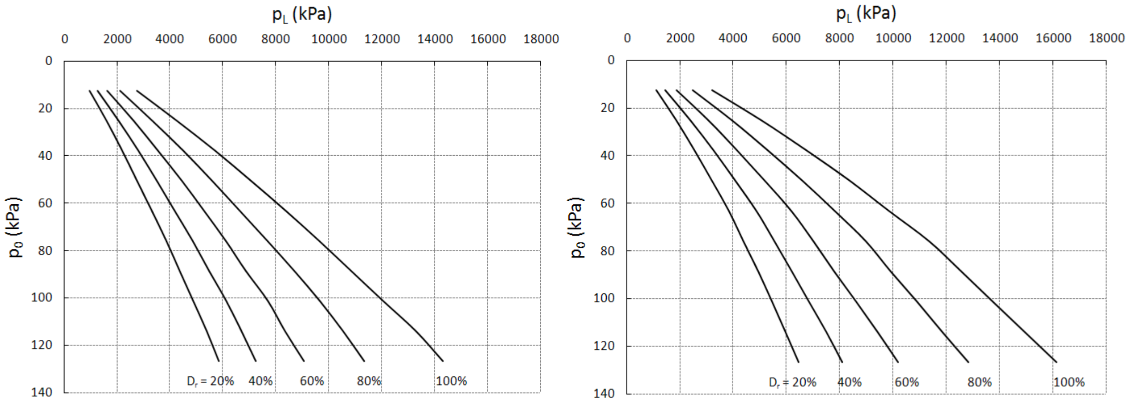

(a) (b)

Figure 4-6: Influence of failure criteria on the limit pressure for $ø_{cs} = 29^{\circ}$.
(a) v_{λ} : M : M-C (b) v_{λ} : M : SMP

Based upon the preceding simulations, it was concluded that an analysis using a combination of Bolton's friction angle model and the Mohr-Coulomb failure criterion would produce the lowest possible output for the limit pressure as seen in Figure 4-7 (a). Alternatively, maximum output is obtained when the friction angle model using v_{λ} and the SMP failure criterion are used in combination as seen in Figure 4-7 (b).

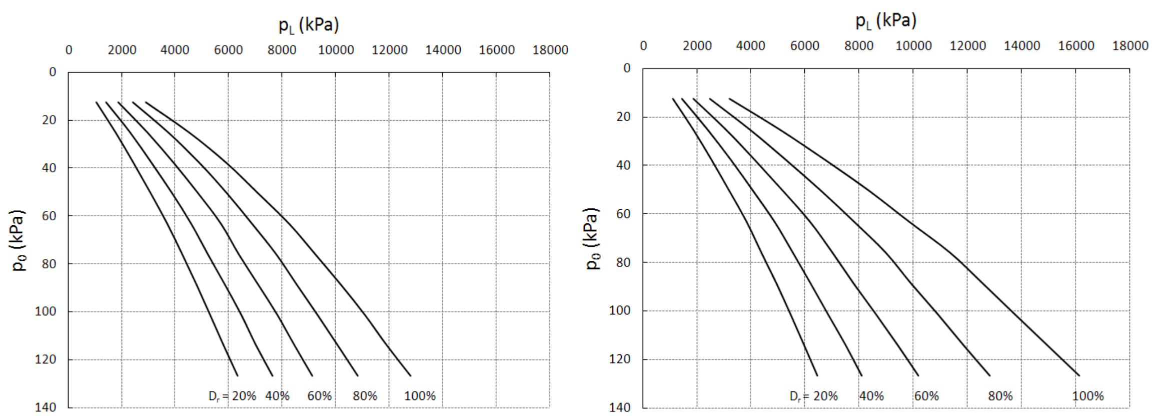

(a) (b)

Figure 4-7: Minimum and maximum output of limit pressure for $ø_{cs} = 29^{\circ}$.
(a) B : M : M-C (b) v_{λ} : M : SMP

Deviations of up to 25 percent were observed between the combinations that produced the maximum and minimum values of limit pressure. The largest deviations occurred for large values of confining stress and relative density. For low confining stresses, simulations using either combination predicted very similar limit pressures.

Based upon the preceding results, combinations using Bolton's friction angle model and the Mohr-Coulomb failure criterion over predicted measured limit pressures by a factor of two. It should also be noted that this same combination produced the lowest predictions in the comparative analysis. Therefore, in order to minimize the difference between the predicted and measured limit pressures using the algorithm presented here, the aforementioned combination should be implemented. Any other combination will produce results which over-predict by a larger extent.

Chapter Five

Conclusions and Recommendations

5.1 Conclusions

A comprehensive investigation into drained cylindrical cavity expansion behavior in sands has been presented. The finite difference model of Salgado et al. (1997, 2001, 2007) was modified so that friction angle models, flow rules and failure criteria could be easily interchanged. From this model, limit pressures were calculated for varying depths and relative densities.

Based on observations made by Lancellotta (1995), the parameter v_λ was used to empirically model changes in the friction angle. It was shown that cavity expansion analysis results using this empirical model were slightly larger in magnitude than those obtained from analyses using the model of Bolton (1986). Dissimilarities can be attributed to Bolton having performed a regression analysis on 10 different sands to obtain an empirical relation whereas the model used in this study was developed using test data from Ticino sand exclusively. Difficulty was encountered when implementing the model of Been & Jefferies (1985), thus corresponding results were not included in this study. The exponential form of the Been and Jefferies' model contrasts with the two alternative relations which assume linear dependence, and as such, led to convergence difficulties.

Similar studies by Salgado et al. (1997, 2001, 2007) and Hao et al. (2010) used Rowe's flow rule exclusively, whereas this study chose to also implement the original cam-clay, modified cam-clay and the flow rule proposed by Muhunthan & Sasiharan (2007). It was found that the choice of flow rule had little impact on the results obtained from the algorithm. These observations are consistent with findings by Silvestri et al. (2009) where the Nova, Rowe, Cam-clay and Sawtooth flow rules were implemented into a cavity expansion model assuming drained and plane strain conditions. Silvestri and his colleagues found that the aforementioned flow rules produced very similar plastic responses.

Integration of the SMP failure criterion into the algorithm produced slightly larger values of limit pressure than that of the Mohr-Coulomb failure criterion. From these observations, it was concluded that neglecting effects due to the intermediate stress produces conservative values for the limit pressure. Thus, the Mohr-Coulomb criterion is an attractive option for design applications since it produces worst case scenario predictions for strength and is significantly simpler to implement than the SMP criterion.

After performing linear regression analyses between values of the limit pressure predicted from the algorithm presented here and measured values of the limit pressure (Ghionna et al. 1989), it was observed that the algorithm over predicted the limit pressure by approximately 68 percent. For large confining stress conditions, this result was expected since the effects of particle crushing were neglected in this study. Hao et al. (2010) presented results from a cavity expansion algorithm which was very similar to that used in this study. The fundamental difference being how particle crushing was chosen to be modeled using the critical state concepts presented by Russell & Khalili (2006). They found that predicted values of the limit pressure that accounted for particle crushing were approximately 40 percent less than corresponding predictions which neglected particle crushing.

The limit pressure curves obtained from the algorithm proposed in this study can be used to interpret pressuremeter data obtained from sands in the field. If the depth of a pressuremeter investigation is known as well as the measured limit pressure, values for the initial in-situ relative density can be approximated. In addition, results for the ratio R/a can be used to gage the plastic influence range for a driven pile with a known diameter. Such information could be used to assess interactions between individual piles within a grouping. Results presented here assumed that the soil mass being modeled was homogenous, but it should be noted that the algorithm can easily be used to obtain results for layered soil profiles as well.

Limit pressure predictions are not only applicable to the pressuremeter but that of the CPT as well. Past research efforts have shown that the limit pressure correlates well with the cone resistance q_c. The limit pressure analysis presented here can be used in conjunction with models proposed by Salgado & Prezzi (2007) or Yu et al. (1996) to predict values of q_c. This has practical applications in engineering practice because measured values of q_c can be used to back calculate limit pressures for ranges in relative density.

5.2 Recommendations for Future Research

The concepts presented in this study can be further extended into these additional research topics:

1. Drained cavity expansion from an initial finite radius which includes particle crushing effects.
2. Cavity expansion in clays using the finite difference model.
3. Comparisons between pressuremeter data obtained in the field and data predicted using finite difference modeling.
4. Investigation into how the friction angle model using v_λ varies for different sand types.
5. Investigation into a new empirical model for predicting the friction angle which is parameterized by the volume decrease potential V_d first proposed by Ishihara & Watanabe (1976).

APPENDIX A

IN-SITU PENETRATION DEVICES

Pressuremeter (PMT):

Since it was introduced in the mid 50's by Professor Louis Menard, the pressuremeter has slowly become recognized as a powerful tool for measuring in-situ strength characteristics of soil. From this test, important soil stiffness properties can be measured directly in the field without having to infer such properties from laboratory data that can be significantly influenced by soil disturbance. Soil properties that can be directly measured include the shear modulus, elastic modulus and the limit pressure which represents the lateral bearing capacity of the soil (Robertson 1985). The theory behind the pressuremeter test is founded on elastic-plastic continuum mechanics and there have been significant advances in understanding cavity expansion theory in clays or "cohesive soils". However, due to the dilatant behavior which sands exhibit under shearing, significant research is still required to develop a strong theoretical understanding of cavity expansion in coarse grained geomaterials.

The pressuremeter device is essentially a cylindrical probe that has the capability to expand its walls laterally via a hydraulically pressurized membrane. The pressuremeter is positioned inside the shaft of a borehole. The test is initialized by expanding the cover of the device laterally in order to make contact with the wall of the borehole. After contact has been made, the membrane will continue to be pressurized and data acquisition will commence. Radial displacements and membrane pressures are relayed to the surface throughout the course of the test and stored in a read-out unit. Testing is typically terminated when either a radial strain of approximately 20 percent is reached or the membrane pressure remains constant with increasing radial displacement (Waisnor et al. 2001).

Stress-strain curves can be generated from the displacement and pressure data obtained from pressuremeter field tests. Examples of stress-strain curves that would be typical of field tests are shown in Figure A-1. For each curve in Figure A-1, a limit pressure has clearly been reached as evidenced by the steady pressure readings past a limiting radial strain. It can also be seen that each curve has a set of three points where the pressuremeter was unloaded then reloaded in order obtain measurements of the shear modulus. Inconsistencies in the stress-strain curves have been observed depending on the type of pressuremeter used in the characterization.

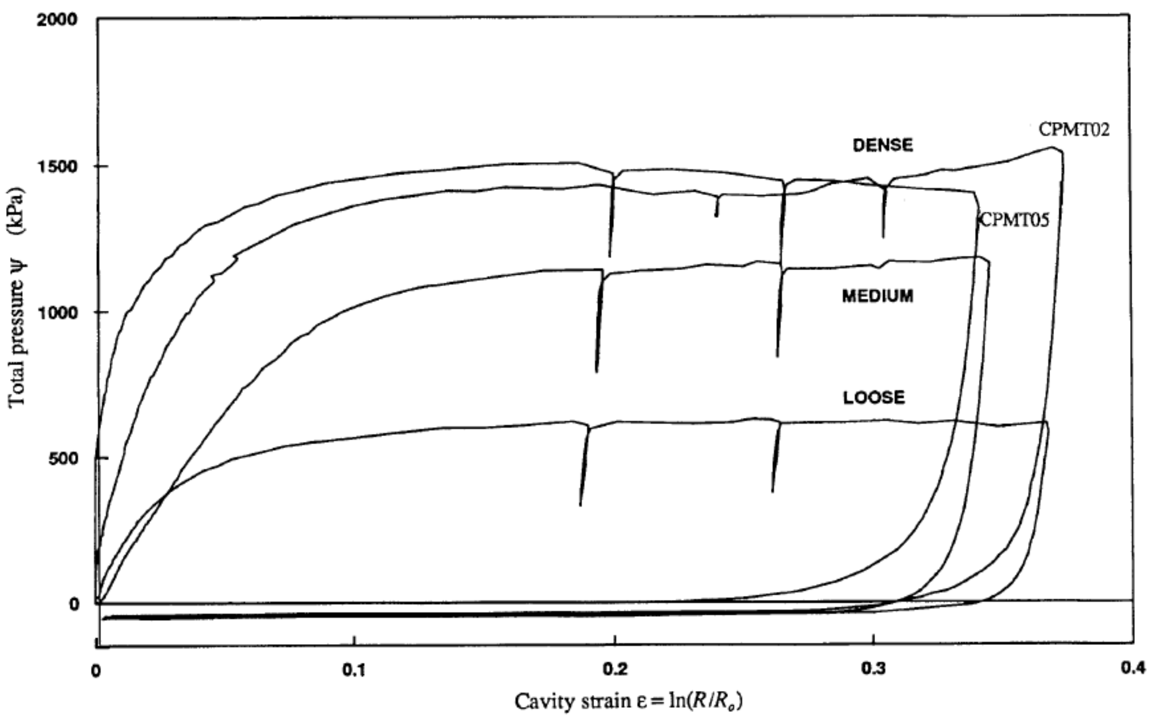

Figure A-1: Calibration chamber plots of cavity pressure versus cavity strain (after Schnaid 1990).

There are three general variations of the pressuremeter that are utilized during a field investigation. The first variation is a *borehole pressuremeter* (Figure A-2 (a)) which can be inserted into an existing borehole. This implies that in order for the borehole pressuremeter to be used, complementary augering equipment is required. In situations where a borehole pressuremeter is used, drillers must auger to a depth of interest then remove their equipment from the borehole in order to re-insert the test equipment. If casings are not used in the drilling process, relaxation of the borehole will occur. This is an undesired consequence as the resulting test data will not reflect accurate in-situ conditions due to soil disturbance. The borehole pressuremeter is generally not practical for use in sands due to the probable instability of the borehole. This limitation has led engineers to modify this original pressuremeter design.

The *self-boring pressuremeter* (Figure A-2 (b)) has the capability of boring itself to a desired test depth, as the name implies. This reduces the need for additional drilling equipment and has the advantage of reducing soil disturbance. When a self-boring pressuremeter bores to a depth of interest, tests can be performed almost immediately which has the advantage of capturing fairly representative initial lateral stress states. Beneficial implications for design become apparent because coefficients of lateral earth pressure can now be directly measured as well as overconsolidation ratios which are known to strongly influence soil behavior. How accurately the test data can represent undisturbed conditions is still debatable due to the fact that soil disturbance is still present, only to a lesser extent compared to the aforementioned borehole pressuremeter (Schnaid 1990).

The third variation is the *displacement pressuremeter*, also known as the *cone pressuremeter* (Figure 1-2 (c)). The displacement pressuremeter is pushed into the ground, rather than augered, and is typically located up-shaft from a cone penetrometer. Analysis of data produced from this device needs to account for the displacement of soil due to pushing the cone into the soil (Schnaid 1990). This device has the added benefit of being able to simultaneously interpret pressuremeter data with tip and shaft resistances recorded by the cone penetrometer.

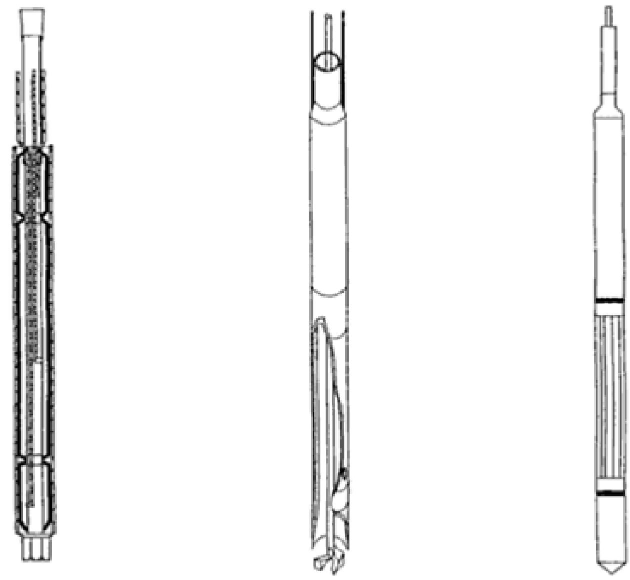

(a) (b) (c)

Figure A-2: Pressuremeter variations (modified after Clough et al. 1990).

It is important to recognize that the displacement pressuremeter initiates cavity expansion from an initial radius of zero whereas other variations start at a finite radius greater than zero. The cavity expansion algorithm presented in this study attempts to simulate readings that could be anticipated for a displacement pressuremeter type investigation. However, the only results that are expected to be different from that of the borehole and self-boring pressuremeters are the values for the minimum cavity radius required to reach the limit pressure. The type of pressuremeter an engineer chooses to use for a site investigation will not influence the value of the measured limit pressure. For any initial state of density and stress within a soil mass, there is only one unique value of the limit pressure.

Measurements of the limit pressure of soil can be very insightful when in the design process for a deep foundation. As stated previously, the limit pressure is a measure of the bearing capacity of a soil and efforts have been made to correlate pressuremeter curves with load displacement (p-y) curves for laterally loaded pile foundations as shown in Figure A-3. Large lateral loads and moments are typically induced by earthquakes, large wind loads and the force induced by the flow of water; all of which are serious engineering concerns. Several methods have been proposed to predict pile movement subjected to lateral loads using pressuremeter data and calculations for critical depth. Despite the implementation of the controversial critical depth calculation (Fellenius & Altaee 1995), some of these methods have been proven to be reliable predictors when compared to full scale load testing (Briaud et al. 1984, Robertson et al. 1983).

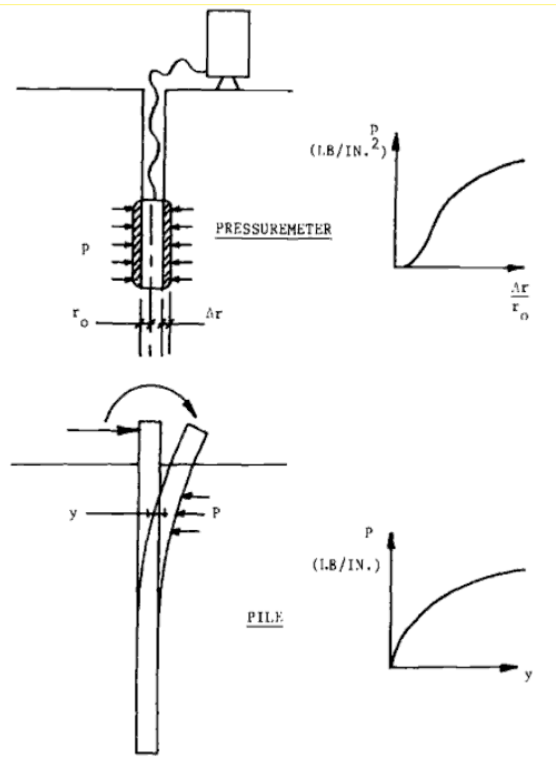

Figure A-3: Pressuremeter and laterally loaded pile analogy (modified after Briaud et al. 1984).

There are still many refinements that need to be made in the understanding and implementation of the pressuremeter device in the engineering sector, especially in situations that involve coarse-grained soils. This study explores cylindrical cavity expansion behavior of sands from a theoretical standpoint so that pressuremeter investigations in sands can be interpreted with a higher degree of confidence.

Cone Penetrometer (CPT):

The cone penetrometer test (CPT) involves hydraulically pushing a steel cone equipped with load cells vertically downward into a soil stratum. Pressure readings from the tip of the penetrometer as well as friction readings along the sleeve located directly up from the cone are relayed to data acquisition equipment at the surface. From these readings, a variety of subsurface characteristics can be inferred. Pore pressures can also be measured by integration of a piezo element behind the cone. This variation is known as a piezo-cone (CPTU) from which effective measurements of resistance are obtained. Figure A-4 displays a rig equipped with a piezo-cone and a pressuremeter, also known as a displacement pressuremeter.

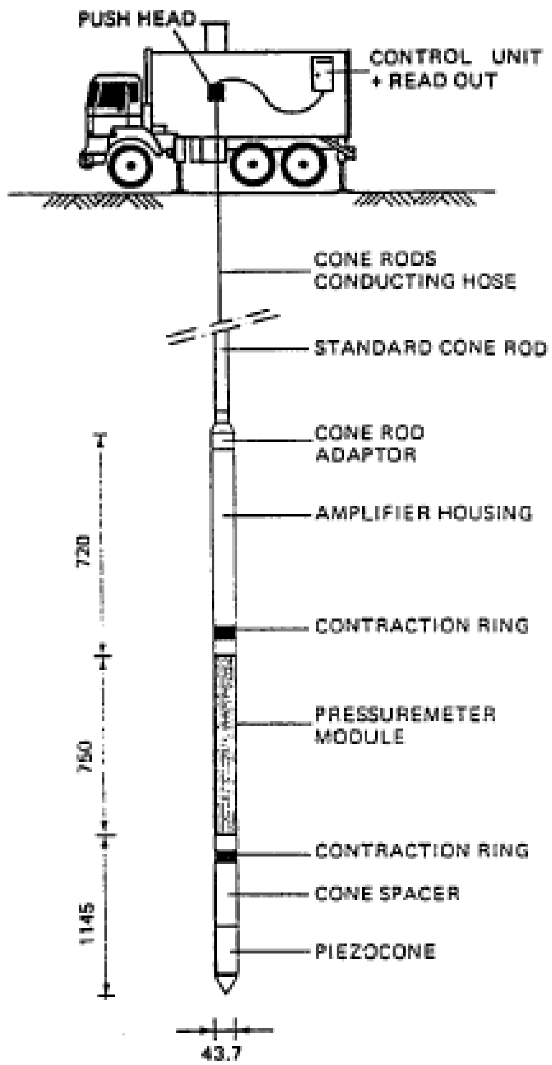

Figure A-4: Piezo-cone with pressuremeter (after Withers et al. 1989).

Researchers have observed strong correlations with the limit pressure and the cone tip resistance q_c (Yu et al. 1996). As such, a significant amount of effort has been invested in trying to understand this relation in detail. Yu et al. (1996) proposed an empirical relation which correlated the ratio of q_c to the limit pressure with the state parameter ξ. Later, Salgado et al. (1997, 2007) approximated values for q_c from the limit pressure by assuming a plane strain slip mechanism just below the tip of the cone. From such relations, limit pressures can be back calculated from data for q_c or vice-versa.

APPENDIX B

DERIVATIONS FOR THE DEVIATOR STRAIN USING THE WORK EQUATION

Triaxial Compression:

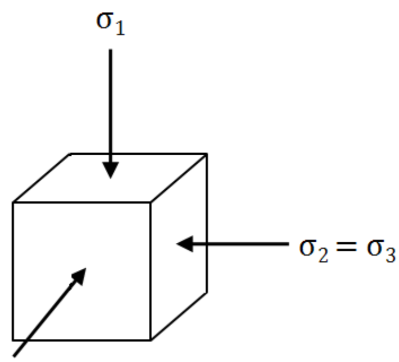

Figure B-1: Triaxial loading.

The work equation can be shown as:

$$\Delta W = \sigma_1 d\varepsilon_1 + 2\sigma_3 d\varepsilon_3 = p d\varepsilon_v + q d\varepsilon_s = \frac{1}{3}(\sigma_1 + 2\sigma_3)d\varepsilon_v + (\sigma_1 - \sigma_3)d\varepsilon_s \quad \text{(B-1)}$$

$$d\varepsilon_v = d\varepsilon_1 + 2d\varepsilon_3 \quad \text{(B-2)}$$

Combine B-1 and B-2 to obtain:

$$\sigma_1 d\varepsilon_1 + 2\sigma_3 d\varepsilon_3 = \frac{1}{3}(\sigma_1 + 2\sigma_3)(d\varepsilon_1 + 2d\varepsilon_3) + (\sigma_1 - \sigma_3)d\varepsilon_s \quad \text{(B-3)}$$

B-3 can then be solved for $d\varepsilon_s$:

$$d\varepsilon_s = \frac{2}{3}(d\varepsilon_1 - d\varepsilon_3) \quad \text{(B-4)}$$

Bi-axial Compression:

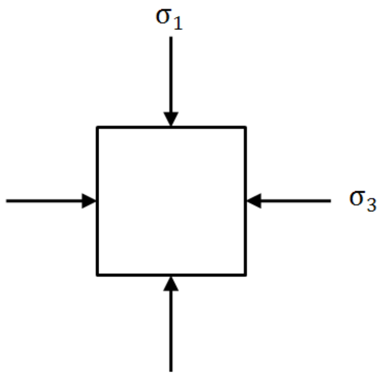

Figure B-2: Bi-axial loading.

The work equation becomes:

$$\Delta W = \sigma_1 d\varepsilon_1 + \sigma_3 d\varepsilon_3 = sd\varepsilon_v + td\varepsilon_s = \frac{1}{2}(\sigma_1 + \sigma_3)d\varepsilon_v + \frac{1}{2}(\sigma_1 - \sigma_3)d\varepsilon_s \quad \text{(B-5)}$$

$$d\varepsilon_v = d\varepsilon_1 + d\varepsilon_3 \quad \text{(B-6)}$$

Combine B-5 and B-6 to obtain:

$$\sigma_1 d\varepsilon_1 + \sigma_3 d\varepsilon_3 = \frac{1}{2}(\sigma_1 + \sigma_3)(d\varepsilon_1 + d\varepsilon_3) + \frac{1}{2}(\sigma_1 - \sigma_3)d\varepsilon_s \quad \text{(B-7)}$$

B-7 can then be solved for $d\varepsilon_s$:

$$d\varepsilon_s = d\varepsilon_1 - d\varepsilon_3 \quad \text{(B-8)}$$

APPENDIX C

DERIVATIONS FOR ROWE'S FLOW RULE

Triaxial Compression:

For a purely frictional material, Rowe (1962) proposed the following expression which relates the energy introduced to a unit volume of soil (E_{in}) against the energy dissipated (E_{out}) as:

$$\frac{E_{in}}{E_{out}} = \frac{\sigma_1}{\sigma_3} = N\left(1 - \frac{d\varepsilon_v}{d\varepsilon_1}\right) \tag{C-1}$$

For triaxial compression conditions, C-1 can be simplified as:

$$\frac{E_{in}}{E_{out}} = \frac{\sigma_1 d\varepsilon_1}{-2\sigma_3 d\varepsilon_3} = N \tag{C-2}$$

Rearrange C-2 to obtain:

$$\frac{\sigma_1}{\sigma_3} = -2N\frac{d\varepsilon_3}{d\varepsilon_1} \tag{C-3}$$

The stress ratio η for triaxial conditions is:

$$\eta = \frac{q}{p} = \frac{\sigma_1 - \sigma_3}{\frac{1}{3}(\sigma_1 + 2\sigma_3)} = \frac{{}^{\sigma_1}\!/_{\sigma_3} - 1}{\frac{1}{3}\left({}^{\sigma_1}\!/_{\sigma_3} + 2\right)} \tag{C-4}$$

Combining C-3 and C-4:

$$\eta = \frac{1 - 2N\frac{d\varepsilon_3}{d\varepsilon_1}}{\frac{1}{3}\left(2 - 2N\frac{d\varepsilon_3}{d\varepsilon_1}\right)} \tag{C-5}$$

Rearranging C-5 to obtain:

$$\frac{d\varepsilon_3}{d\varepsilon_1} = \frac{1 + \frac{2}{3}\eta}{2N\left(\frac{\eta}{3} - 1\right)} \tag{C-6}$$

Using the strain equations derived in Appendix B, the expression for dilatancy can be cast as:

$$\frac{d\varepsilon_v}{d\varepsilon_s} = \frac{d\varepsilon_1 + 2d\varepsilon_3}{\frac{2}{3}(d\varepsilon_1 - d\varepsilon_3)} = \frac{1 + 2\frac{d\varepsilon_3}{d\varepsilon_1}}{\frac{2}{3}\left(1 - \frac{d\varepsilon_3}{d\varepsilon_1}\right)} \tag{C-7}$$

When C-6 and C-7 are combined, the following flow rule results:

$$\frac{d\varepsilon_v}{d\varepsilon_s} = \frac{6\eta - 9N + 3N\eta + 9}{2N\eta - 6N - 2\eta - 3} \tag{C-8}$$

At the critical state *and* assuming Mohr-Coulomb type failure:

$$N = \frac{1 + \sin\text{ø}_{cs}}{1 - \sin\text{ø}_{cs}} \tag{C-9}$$

where $\sin\text{ø}_{cs}$ for triaxial compression conditions is represented by:

$$\sin\text{ø}_{cs} = \frac{3M_{TX}}{6 + M_{TX}} \tag{C-10}$$

Combining C-8, C-9 and C-10 results in Rowe's flow rule for triaxial conditions assuming Mohr-Coulomb failure (Yang & Li 2004, Chang & Yin 2010):

$$\frac{d\varepsilon_v}{d\varepsilon_s} = \frac{9(M_{TX} - \eta)}{3M_{TX} - 2M_{TX}\eta + 9} \tag{C-11}$$

Bi-axial Compression:

Rowe's energy relation for bi-axial compression becomes:

$$\frac{E_{in}}{E_{out}} = \frac{\sigma_1 d\varepsilon_1}{-\sigma_3 d\varepsilon_3} = N \tag{C-12}$$

Rearrange C-12 to obtain:

$$\frac{\sigma_1}{\sigma_3} = -N\frac{d\varepsilon_3}{d\varepsilon_1} \tag{C-13}$$

The stress ratio η for bi-axial stress conditions is:

$$\eta = \frac{t}{s} = \frac{\sigma_1 - \sigma_3}{\sigma_1 + \sigma_3} = \frac{\sigma_1/\sigma_3 - 1}{\sigma_1/\sigma_3 + 1} \tag{C-14}$$

Combine C-13 and C-14:

$$\eta = \frac{1 + N\frac{d\varepsilon_3}{d\varepsilon_1}}{N\frac{d\varepsilon_3}{d\varepsilon_1} - 1} \tag{C-15}$$

Rearrange C-15 to obtain:

$$\frac{d\varepsilon_3}{d\varepsilon_1} = \frac{\eta + 1}{N(\eta - 1)} \tag{C-16}$$

The bi-axial strain expression for dilatancy is:

$$\frac{d\varepsilon_v}{d\varepsilon_s} = \frac{d\varepsilon_1 + d\varepsilon_3}{d\varepsilon_1 - d\varepsilon_3} = \frac{1 + \frac{d\varepsilon_3}{d\varepsilon_1}}{1 - \frac{d\varepsilon_3}{d\varepsilon_1}} \tag{C-17}$$

The following flow rule is attained when C-16 is combined with C-17:

$$\frac{d\varepsilon_v}{d\varepsilon_s} = 1 - \frac{2\eta + 2}{N + \eta - N\eta + 1} \tag{C-18}$$

At the critical state and assuming Mohr-Coulomb type failure:

$$N = \frac{1 + \sin\phi_{cs}}{1 - \sin\phi_{cs}} \tag{C-19}$$

$\sin\phi_{cs}$ for bi-axial conditions is represented by:

$$\sin\phi_{cs} = M_{BX} \tag{C-20}$$

Combining C-18, C-19 and C-20 results in Rowe's flow rule for bi-axial loading assuming Mohr-Coulomb failure (Gutierrez & Wang 2009):

$$\frac{d\varepsilon_v}{d\varepsilon_s} = \frac{\eta - M_{BX}}{M_{BX}\eta - 1} \tag{C-21}$$

APPENDIX D

DERIVATIONS FOR ORIGINAL CAM-CLAY AND MODIFIED CAM-CLAY FLOW RULES

Original Cam-clay (OCC):

Roscoe & Schofield (1963) provided the following energy relation for soils:

$$\Delta W = p d\varepsilon_v + q d\varepsilon_s = pMd\varepsilon_s \tag{D-1}$$

Equation D-1 can be rearranged to form the original cam-clay flow rule:

$$\frac{d\varepsilon_v}{d\varepsilon_s} = M - \frac{q}{p} = M - \eta \tag{D-2}$$

Modified Cam-clay (MCC):

For modeling applications, it was found that the yield surface produced by the OCC flow rule allowed for three possible stress path directions for isotropic consolidation assuming associated behavior. Roscoe & Burland (1968) solved this issue by modifying the dissipation function to include the volumetric strain.

$$\Delta W = p d\varepsilon_v + q d\varepsilon_s = p\sqrt{(d\varepsilon_v)^2 + (Md\varepsilon_s)^2} \tag{D-3}$$

Equation D-4 can be rearranged to obtain the modified cam-clay flow rule:

$$\frac{d\varepsilon_v}{d\varepsilon_s} = \frac{M^2 - \left(\frac{q}{p}\right)^2}{2\eta} = \frac{M^2 - \eta^2}{2\eta} \tag{D-4}$$

Note: The preceding equations are for triaxial conditions, but q and p can be replaced by t and s in equations D-1 and D-3 in order to arrive at the same flow rule equations. Therefore, the only differences lie in how η and M are defined.

References

Been, K. and Jefferies, M. (1985). A state parameter for sands. *Geotechnique* 35(2), 99-112.

Been, K. and Jefferies, M. (2006). *Soil liquefaction: a critical state approach*. London: Taylor & Francis.

Bishop, A. W. (1966) "The strength of soils as engineering materials." 6th Rankine lecture. *Geotechnique,* 16(9), 91–130.

Bolton, M. D. (1986). "The strength and dilatancy of sands." *Geotechnique* 36(1), 65-78.

Briaud, J. L., Smith, T., and Meyer, B. (1984) "Laterally loaded piles and the pressuremeter: comparison of existing methods." *Laterally loaded deep foundations: analysis and performance*, ASTM STP 835, J.A. Langer, E.T. Mosley, and C.D. Thompson, Eds., American society for testing and materials, pp. 97-111.

Carter, J.P., Booker, J. R., and Yeung, S.K. (1986). "Cavity expansion in cohesive-frictional soils." *Geotechnique*, 36, 349-353.

Carter, J. P. and Yu, H. S. (2002). "Rigorous similarity solutions for cavity expansion in cohesive-frictional soils." *The international journal of geomechanics*, 2(2), 233-258.

Chang, C. S., and Yin, Z. Y. (2010). "Modeling stress-dilatancy for sand under compression and extension loading conditions." *Journal of engineering mechanics*, 136(6), 777.

Clough, G. W., Briauld, J. L. and Hughes, J. M. O. (1990). "The development of pressuremeter testing." *Proceedings of the third international symposium on pressuremeters*, 25-45.

Collins, I. F., Pender, M. J. and Wang, Y. (1992). "Cavity expansion in sands under drained loading conditions." *International journal for numerical and analytical methods in geomechanics*, 16(1), 3-23.

Collins, I. F. and Muhunthan, B. (2003). "On the relationship between stress-dilatancy, anisotropy, and plastic dissipation for granular materials." *Geotechnique London*, 53, 611-618.

Dafalias, Y. F. and Li, X. S. (2001). "Dilatancy for cohesionless soils." *Geotechnique London*, 51, 729-730.

Davis, E. H. (1969). "Theories of plasticity and the failure of soil masses." *Soil Mechanics Selected Topics*, Chap. 6, Lee, I. K., Ed., London, Butterworth, 341-380.

Drucker, D.C. (1959) “A definition of stable inelastic material. Transactions of the ASME.” *Journal of applied mechanics*, 26(1), 101-106.

Fellenius, B. H. and Altaee, A. A. (1996). “Critical depth: how it came into being and why it does not exist.” *Proceedings - institution of civil engineers geotechnical engineering.* 244-245.

Ghionna, V., Jamiolkowski, M., Lancellotta, R. and Manassero, M (1989). "Limit pressure of pressuremeter tests". *Proc. of 12th ICSMFE, Rio De Janeiro*.

Griffiths, D. V. and Huang, J. (2009). “Observations of the extended matsuoka-nakai failure criterion”, *International journal for numerical and analytical methods in geomechanics*, 33, 1889-1905.

Gutierrez, M., and Wang, J. (2009). “Non-coaxial version of rowe's stress-dilatancy relation.” *Granular matter,* 11(2), 129-137.

Hao, D., Luan, M., Li, B. and Chen, R. (2010). “Numerical analysis of cylindrical cavity expansion in sand considering particle crushing and intermediate principal stress.” *Transactions- Tianjin University*, 16(1), 68-74.

Hardin, B. and Black, W. (1968). “Shear modulus and damping of soils.” *Journal of soil mechanics and foundations division*, 94(2), 353-369.

Houlsby, G. T. and Carter, J. P. (1993). “The effects of pressuremeter geometry on the results of tests in clay.” *Geotechnique*, 43, 567–576.

Ishibashi, I. and Zhang, X. (1993). “Unified dynamic shear moduli and damping ratios of sand and clay.” *Soils Found.*, 33(1), 182-191.

Ishihara, K. and Watanabe, T. (1976). “Sand liquefaction through volume decrease potential.” *Soils and Foundations*, 16(4), 61-70.

Jefferies, M. G. (1993). “NorSand: a simple critical state model for sand.” *Geotechnique,* 43, 91-103.

Lade, P.V. and Duncan, J.M. (1975). “Elastoplastic stress-strain theory for cohesionless soil.” *J. geotechnical engineering division, ASCE*, 101(GT10), 1037-1053.

Lancellotta, R. (1995). *Geotechnical engineering*. Rotterdam: A.A. Balkema.

Matsuoka, H. and Nakai, T. (1974). “Stress-deformation and strength characteristics of soil under three different principal stresses.” *Proc. of JSCE*, 232, 59-70.

Muhunthan, B. and Sasiharan, N. (2007). “States of dilatancy and plasticity modeling of granular media.” *Proc. first Sri Lankan Geotechnical Society SLGS international conference on soil and rock engineering, Colombo, Sri Lanka*.

Palmer, A. C. (1972). “Undrained plane-strain expansion of a cylindrical cavity in clay: a simple interpretation of the pressuremeter test.” *Geotechnique*, 22(3), 451-457.

Reynolds, O. (1885). “On the dilatancy of media composed of rigid particles in contact. With experimental illustrations.” *The London, Edinburgh and Dublin philosophical magazine and journal of science*, Vol. XX, 5th series, 469-481.

Robertson, P. K., Hughes, J. M. O., Campanella, R. G. and Sy, A. (1984) “Design of laterally loaded displacement piles using a driven pressuremeter.” *Laterally loaded deep foundations: analysis and performance. ASTM STP 835*, A. Langer, E. T. Mosley, and C. D. Thompson, Eds., American society for testing and materials, 229-238.

Robertson, P. K. and University of British Columbia (1985). *Design of laterally loaded piles using the pressuremeter*. Vancouver, B.C: Dept. of Civil Engineering, University of British Columbia.

Roscoe, K. H., Schofield, A. N. and Wroth, C. P. (1958). “On the yielding of soils.” *Geotechnique*, 8(1), 22-53.

Roscoe, K. H. and Schofield, A. N. (1963). “Mechanical behaviour of an idealised ‘wet’ clay.” *Proc. 2nd european conf. on soil mechanics and foundation engineering,Wiesbaden*, 1, 47-54.

Roscoe K.H. and Burland J.B. (1968), “On the generalised stress-strain behaviour of ‘wet’ clay.” *Eng. plasticity*, Cambridge Univ. Press, 535-609

Rowe, P. W. (1962). “The stress-dilatancy relation for static equilibrium of an assembly of particles in contact.” *Proceedings of the royal society of London. series A, mathematical and physical sciences*, 269(1339), 500-527.

Russell, A. R. and Khalili N. (2006). “On the problem of cavity expansion in unsaturated soils.” *Computational mechanics*, 37(4), 311-330.

Salgado, R., Boulanger, R. W. and Mitchell, J. K. (1997). “Lateral stress effects on CPT liquefaction resistance correlations.” *Journal of geotechnical and geoenvironmental engineering*, 123(8), 726-735.

Salgado, R. and Randolph, M. F. (2001). “Analysis of cavity expansion in sand.” *The international journal of geomechanics*, 1(2), 175-192.

Salgado, R. and Prezzi, M. (2007). “Computation of cavity expansion pressure and penetration resistance in sands.” *International journal of geomechanics*, 7(4), 251.

Schnaid, F. (1990). *A study of the cone-pressuremeter test in sand*. Thesis (D.Phil.)-- University of Oxford, 1990.

Schnaid, E. and Houlsby, G. T. (1992). "Measurement of the properties of sand by the cone-pressuremeter tests." *Geotechnique,* London, England, 42(4), 587 -601.

Schofield, A. N. and Wroth, P. (1968). *Critical state soil mechanics*. McGraw-Hill.

Schofield, A. N. and University of Cambridge. (1993). *Original cam-clay*. University of Cambridge, Department of Engineering.

Schofield, A. N. (1998). “The "mohr-coulomb" error.” *CUED/D Soils TR*, 305. Cambridge: Univ., Engineering Department.

Schofield, A. N. (2005). *Disturbed soil properties and geotechnical design*. London: Thomas Telford.

Silvestri, V., Abou-Samra, G., and Bravo-Jonard, C. (2009). “Effect of flow rules and elastic strains on pressuremeter test results in dense sand.” *Canadian geotechnical journal*, 46, 160-167.

Taylor, D. W. (1948). *Fundamentals of soil mechanics*. John Wiley, New York.

Waisnor, B. M., Ducote-Price, A., Jarosz, B., Duncan, M. and Smith, C. J. (2001). “Geotechnical engineering within the piedmont physiographic province, appendix A.” *Report of a study performed by the Virginia Tech Center for Geotechnical Practice and Research*.

Withers, N. J., Howie, J., Hughes, J. M. and Robertson, P. K. (1989). "Performance and analysis of cone pressuremeter tests in sands." *Geotechnique,*London, England, 39(3), 433-454.

Wroth, C.P. (1984) “The interpretation of in situ soil tests.” *Geotechnique*, 34, 449-489.

Wroth Memorial Symposium, Wroth, P., Houlsby, G. T. and Schofield, A. N. (1993). *Predictive soil mechanics: Proceedings of the Wroth Memorial Symposium held at St. Catherine's College, Oxford,* 27-29 July 1992. London: T. Telford.

Yang, J. and Li, X. S. (2004). “State-dependent strength of sands from the perspective of unified modeling.” *Journal of geotechnical and geoenvironmental engineering,* 130(2), 186.

Yu, H. S., Schnaid, F. and Collins, I. F. (1996). “Analysis of cone pressuremeter tests in sands.” *Journal of geotechnical engineering,* 122(8), 623.

Yu, H. S. (2000). *Cavity expansion methods in geomechanics*. Dordrecht: Kluwer Academic Publishers.